Impact of Multiple Radar Wind Profilers Data Assimilation on Convective Scale Short-Term Rainfall Forecasts: OSSE Studies over the Beijing-Tianjin-Hebei region

Juan Zhao[1], Jianping Guo[2*], and Xiaohui Zheng[1]

[1]China Meteorological Administration Training Centre, Beijing, 100081, China

[2]State Key Laboratory of Severe Weather, Chinese Academy of Meteorological Sciences, Beijing, 100081, China

To be submitted to EGU *Geoscientific Model Development*

[*]*Correspondence to*: Jianping Guo (jpguo@cma.gov.cn; jpguocams@gmail.com)

Abstract

The optimal spatial layout of a radar wind profiler (RWP) network for rainfall forecasting, especially over complex terrain, remains uncertain. This study explores the benefits of assimilating vertical wind measurements from various RWP network layouts into convective-scale numerical weather prediction (NWP) through observing system simulation experiments (OSSEs). Synthetic RWP data were assimilated into the Weather Research and Forecasting (WRF) model using the National Severe Storms Laboratory three-dimensional variational data assimilation (DA) system for three southwest (SW)-type heavy rainfall events in the Beijing-Tianjin-Hebei region. Four types of DA experiments were conducted and compared: a control experiment (CTL) that assimilates data solely from the operational RWP network, and three additional experiments incorporating foothill (FH), ridge (RD), and combined foothill-ridge (FH_RD) RWP network layouts. A detailed examination of the 21 July 2023 case reveals that the FH_RD experiment generally exhibits more skillful storm forecasts in terms of areal coverage, storm mode, and orientation, benefiting from refined mesoscale wind analysis. Particularly, in the RD experiment, RWP data assimilation notably reduces wind errors and improves the representation of mesoscale atmospheric features near the Taihang Mountains upstream of Beijing, crucial for convective initiation (CI). Aggregated score metrics across all cases also indicate that both FH and RD experiments offer substantial added value over the operational network alone. Further sensitivity experiments on vertical resolution and maximum detection height indicate that the RWP system configuration with the highest detection height achieves the best performance, while lower detection height degrades forecast quality. These findings highlight the importance of strategic RWP network placement along the Taihang Mountains' ridge and foothill for short-term quantitative precipitation forecast in the Beijing-Tianjin-Hebei region.

1 Introduction

Radar wind profilers (RWPs) are state-of-the-art meteorological observation instruments that provide wind profiings at 6-min intervals with a vertical resolution ranging from 60 to 240 meters, enabling the detection of fine-scale atmospheric dynamic structures throughout the troposphere. Researches have demonstrated the capability of RWP to observe the evolution of mesoscale cyclonic circulations, shear lines, and low-level jets (LLJs), which are closely associated with the development of heavy rainfall and convection (Dunn, 1986; Guo et al., 2023; Liu et al., 2003; Wang et al., 2023; Zhong et al., 1996). The wind observations from RWPs are expected to improve initial conditions and severe weather forecasts for convective-scale numerical weather prediction (NWP) through data assimilation (DA). Significant progress has been made in RWP data assimilation, resulting in wind analysis error reduction and short-term forecast skill enhancement (Benjamin et al., 2004; Bouttier, 2001; Ishihara et al., 2006; Liu et al., 2022; St-James & Laroche, 2005; Wang et al., 2022; Zhang et al., 2016). Furthermore, efforts in developing quality control and observation operator schemes are also critical to ensuring the reliability of the observations and enhancing assimilation effectiveness (Wang et al., 2020; C. Wang et al., 2023; Zhang et al., 2016; Zhang et al., 2017).

In China, the deployment of a nationwide RWP network initiated in 2008, with over 260 sites established by the end of 2024. These sites primarily utilize the 1290 MHz Doppler radar to monitor the lower and middle atmosphere (Liu et al., 2020). Currently, the nationwide RWP network is unevenly distributed: the spatial concentration of RWP sites over densely populated metropolitan regions, such as the Beijing–Tianjin–Hebei region, Yangtze River Delta, and Pearl River Delta, are above the national average, while the other regions, especially in west-central China, are lagged behind. Notably, in regions where observation data is relatively abundant, there is still an issue of uneven spatial distribution of stations, mainly due to the terrain complexity. Taking the RWP network in the Beijing–Tianjin–Hebei (BTH) region as an example, seven RWPs are deployed in Beijing within an area of approximately 100 km × 100 km, while there are only 11 profilers in the whole Hebei province (Wang et al., 2022; refer to blue stars in Fig. 3).

Accurate short-term forecasts of heavy rainfall are crucial for mitigating the risks posed by severe weather events in the BTH region, one of China's most densely populated and economically vital areas. The BTH region includes the cities of Beijing and Tianjin, and the Hebei Province, and is

bounded by the Taihang Mountains to the west and Bohai Bay to the east (Fig. 3). Its complex terrain features with high elevations in the northwest and north, gradually transitioning into plains in the south and east. The dominant weather circulations affecting heavy rainfall in the BTH region include the cold vortex, the cold trough, and the trough-anticyclone patterns (Sheng et al., 2020; Zhao et al., 2018; Zhou et al., 2018). The complex underlying surface and the interaction with synoptic- and mesoscale weather processes make the initiation and maintenance mechanisms of convective systems in the BTH region highly unique. Convective initiation (CI) is especially difficult to predict due to local environmental uncertainties and the rapid evolution of meteorological variables. The existing RWP network is mainly located in urban and lowland areas (Fig. 3, blue stars), while the mountainous regions like the Taihang Mountains, where significant terrain-induced convection occurs, are in shortage of sufficient wind profile observations (Liu et al., 2020). These observational gaps can lead to suboptimal initial conditions in NWP models, thereby reducing the accuracy of short-term precipitation forecasts. Therefore, optimizing the distribution of the RWP network, particularly in the Taihang Mountains, could strengthen the ability to monitor these critical regions and improve quantitative precipitation forecasts.

Observation System Simulation Experiments (OSSEs) are widely used to assess the impact of assimilating specific observational data into NWP models (Huang et al., 2022; Zhao et al., 2021a). Previous studies by Zhang & Pu (2010) and Hu et al. (2017) have demonstrated the effectiveness of OSSEs in evaluating the benefits of assimilating RWP data for improving forecasts. Recent research (Bucci et al., 2021; Huo et al., 2023) has also highlighted the advantages of joint assimilation of multiple observational platforms to enhance analysis of convective dynamics, underlining the importance of an optimized RWP network. These OSSEs have provided valuable insights into the strategic RWP site placement to maximize their impact on model performance. To our knowledge, there are few peer-reviewed published research investigating the potential benefit of a RWP network in complex terrain on mesoscale and convective scale weather forecasts (Bucci et al., 2021; Hu et al., 2017; Huo et al., 2023; Zhang and Pu, 2010).

To investigate the impact of a RWP network in complex terrain on heavy rainfall forecasts, we focus on southwest (SW)-type rainfall events associated with southwesterly flow, which constitutes approximately 40% of the total circulation patterns in the BTH region during early summer (Li et al., 2024; Zhou et al., 2018). When warm, moist air from the south meets the cold air from the Taihang

100   Mountains, the terrain causes the air to rise, enhancing convective activity. Meanwhile, the topography

101   of the Taihang Mountains affects the distribution and intensity of the wind field, particularly during

102   severe convective weather events (Li et al., 2024; Sheng et al., 2020). For example, a prior study

103   showed that the quasi-linear convective systems with extreme heavy rainfall primarily occurred at the

104   foothills of the Taihang Mountains or in the plains close to the foothills (Sheng et al., 2020). To address

105   observational gaps, simulated RWP stations are strategically placed along the ridge and foothills,

106   reinforcing the existing operational network.

107   In this study, the following questions will be addressed. How does the assimilation of RWPs

108   from ridge and foothill sites combined with that from operational stations impact heavy rainfall forecast

109   in the BTH region? Do ridge and foothill networks offer added forecast skill over the operational RWP

110   network on short-term convective-scale NWP? Are the benefits of assimilating RWP observations

111   sensitive to the vertical resolution and maximum detection height of profilers? Ultimately, this research

112   aims to provide guidance on optimizing the RWP network to improve forecasting accuracy for heavy

113   rainfall events in the BTH region, thereby enhancing disaster preparedness and response strategies in

114   the region.

115   To address these questions, a series of OSSEs are conducted, assuming a perfect model, using

116   three representative southwest (SW)-type heavy rainfall cases. The remainder of this paper is organized

117   as follows: Section 2 provides an overview of the NWP model and data assimilation system. Truth and

118   background simulation configuration, synthetic observations, experiment design, and evaluation

119   methods are presented in Sect. 3. Section 4 presents the analysis and forecast results for the 21 July

120   2023 case, as well as the aggregated performance across all three cases. Section 5 summarizes the key

121   findings and conclusions.

122   **2 Model and Data Assimilation System**

123   The forecast model used in this study is the version 3.7.1 of the Weather Research and

124   Forecasting Model (WRF) with the Advanced Research WRF (ARW) dynamic solver (WRF-ARW;

125   Skamarock et al., 2008). All DA and forecast experiments are performed on a 1.5-km grid of 408×480

126   horizontal points and 51 vertical levels with a model top at 50-hPa. The domain is centered in the

127   northern part of China covering the Beijing–Tianjin–Hebei region (Fig. 3). The physical

128 parameterizations include the National Severe Storms Laboratory (NSSL) two-moment four-ice

129 category bulk microphysics scheme (Mansell et al., 2010; Mansell and Ziegler, 2013; Ziegler, 1985),

130 the Rapid Radiative Transfer Model (RRTM) longwave radiation scheme (Mlawer et al., 1997), the

131 Dudhia shortwave radiation scheme (Dudhia, 1989), the Rapid Update Cycle (RUC) land surface

132 scheme (Benjamin et al., 2004), and the Yonsei University (YSU) planetary boundary layer scheme

133 (Hong et al., 2006).

134   This research employs the NSSL Experimental Warn-on-Forecast (WoF) 3DVAR system

135 (NSSL3DVAR) (Gao et al., 2013, 2016; Gao & Stensrud, 2014; Wang et al., 2019; Zhuang et al.,

136 2016), specifically designed for convective-scale Numerical Weather Prediction (NWP) and

137 thunderstorm forecasting (Gao et al., 2024; Heinselman et al., 2024). In the NSSL3DVAR system, the

138 analysis is derived by minimizing the cost function defined as the background term J_b and the

139 observation term J_o plus the constraint term J_c:

140
$$J = J_b + J_o + J_c = \frac{1}{2}(\mathbf{x} - \mathbf{x}_b)^T \mathbf{B}^{-1}(\mathbf{x} - \mathbf{x}_b) + \frac{1}{2}(H(\mathbf{x}) - \mathbf{y_o})^T \mathbf{R}^{-1}(H(\mathbf{x}) - \mathbf{y_o}) + J_c, \quad (1)$$

141 where $\mathbf{x}$ and $\mathbf{x}_b$ are the analysis and background state vectors, respectively; H is the observation

142 operator projecting analysis into the observational space; and $\mathbf{y}_o$ is the observation vector. $\mathbf{B}$ is the

143 background error covariance matrix, and $\mathbf{R}$ is the observation error covariance matrix. J_c represents

144 weak constraints which include elastic mass continuity equation and diagnostic pressure equation

145 constraints suitable for convective-scale data assimilation (Gao et al., 2004; Ge et al., 2012). Analysis

146 variables include the three-dimensional wind fields, air pressure, potential temperature, water vapor

147 mixing ratio, and the hydrometeors containing the mass mixing ratios for cloud water, rainwater, ice,

148 snow, and graupel (Gao and Stensrud, 2012).

149   The NSSL3DVAR system assimilates multi-sensor high-resolution observations like radar radial

150 velocity and reflectivity (Gao et al., 2013, 2016), sounding and surface data (Hu et al., 2021), and

151 multiple satellite-retrieved products, such as cloud water path (Pan et al., 2021), total precipitable water

152 (Jones et al., 2018; Pan et al., 2018), atmospheric motion vectors (Mallick and Jones, 2020; Zhao et al.,

153 2021b, 2022), and Geostationary Lightning Mapper (GLM)-derived water vapor (Fierro et al., 2019a;

154 Hu et al., 2020). To enhance the wind field analysis, particularly in the PBL, this study incorporates a

155 RWP assimilation module into the system. Since heavy rainfall and other severe weather events require

156 fast and timely delivery of forecasts and early warning to the public, computationally efficient 3DVAR

157   is quite suitable for the severe weather forecasts by providing highly efficient and rapid updating

158   analysis and forecast, such as 15-min cycle intervals. Our focus is to assess the potential impacts of

159   RWP network enhancements on convective-scale analysis and short-term severe weather prediction

160   with this efficient DA method, so we did not use the ensemble derived background error covariance,

161   which is also incorporated in the variational framework (Gao et al., 2016; Gao & Stensrud, 2014; Wang

162   et al., 2019). The background error covariance matrix used in this study is constructed as the product of

163   a diagonal matrix representing the standard deviations of background errors and a spatial recursive

164   filter (Gao et al., 2004, 2013). The standard deviations for the pressure, potential temperature, relative

165   humidity, zonal and meridional wind components are derived from the statistics of the Rapid Update

166   Cycle (RUC, Benjamin et al., 2004) 3-hour forecasts over several years (Fierro et al., 2019b; Pan et al.,

167   2021). The background error correlations are modeled by the recursive filter described by Purser et al.

168   (2003a, b). The recursive filter can be applied in multiple passes (or outer loops), using different

169   correlation length scales tailored to the scale of the weather systems represented by the assimilated

170   observations.

171   **3. Experimental design**

172   **3.1 Truth run and background run for OSSE**

173   In the OSSE, synthetic RWP observations are generated by adding observation errors to the truth

174   run. To obtain this truth run, the WRF model is initialized with the fifth-generation European Centre

175   for Medium-range Weather Forecasts (ECMWF) atmospheric reanalysis of the global climate (ERA5;

176   Hersbach et al., 2020; Hoffmann et al., 2019), based on the model configuration and parameterization

177   schemes described in Sect. 2. Three SW-type heavy rainfall cases that occurred over the

178   Beijing-Tianjin-Hebei region on 28 June, 12 July, and 21 July of 2023 are selected to construct OSSEs

179   and assess the impact of RWP data observed from different spatial layout schemes on convective

180   initiation and the development of storms. For each case, the model is initialized using the ERA5 data

181   and integrated forward for 15 hours, with the boundary conditions also provided by the hourly ERA5

182   data. An overview of composite reflectivity in the truth simulation from the case on 21 July 2023 is

183   shown in Fig. 1 as an example. This case was characterized by the presence of an upper-level trough

184   gradually moving eastward into the Beijing-Tianjin-Hebei region, accompanied by a corresponding

low-level vortex before the evening of 20 July. Meanwhile, southeasterly winds at the lower levels

continuously transported moisture, leading to high instability in central Hebei, and in the western and

southern parts of Beijing. The combination of easterly winds and topographical effects created

favorable conditions for heavy precipitation. Several discrete storms initiated and developed in

west-central Hebei near the foothills of the Taihang Mountains (Fig. 1a-c). With the westerly trough

moving east and strong southerly airflow strengthening water vapor transport, scattered convective

cells formed in the vicinity of the boundary between Hebei and southwestern Beijing around 1900 UTC

on 20 July, then aggregated and developed into a mesoscale convective system in southwest Beijing

(Fig. 1d-f). Additionally, convective storms in west-central Hebei gradually moved northeastward and

merged with the mesoscale convective system (Fig. 1g). The convective system slowly moved

northeastward and elongated in the southwest–northeast direction (Fig. 1h), persisting across

west-central Beijing until 0900 UTC on 21 July 2023 (Fig. 2).
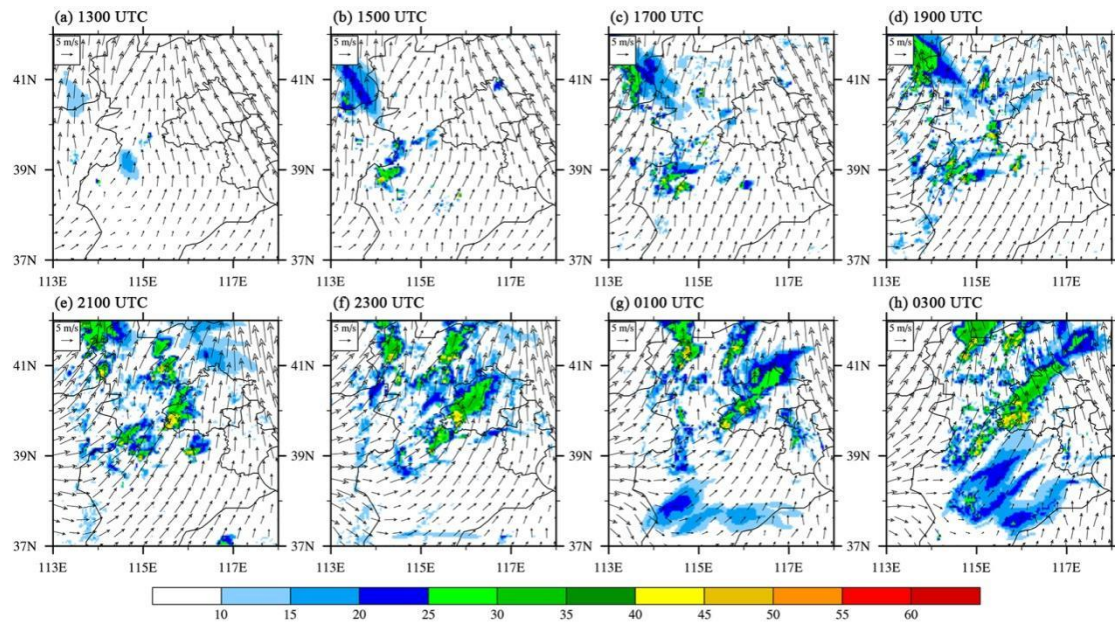
Figure 1. Simulated composite reflectivity (dBZ, shaded) and winds at 700 hPa (m s^{-1}, vectors) for the

truth simulation from 1300 UTC 20 July to 0300 UTC 21 July, 2023.

This study utilizes an OSSE framework with an identical twin setup, where the same numerical

model is used for both the truth simulation and the forecast system. As noted by Hoffman and Atlas

(2016), OSSEs with identical twin setups can lead to overly optimistic assessments of data impacts.

Therefore, the results should be interpreted within the constraint. To mitigate unrealistic assumptions

about observational capabilities and overly optimistic OSSE results, the first-guess background run

(NoDA) uses the National Centers for Environmental Prediction (NCEP) Global Forecast System (GFS)

206   forecasts for initial and boundary conditions, which differ from those of the truth run. The 6-h

207   accumulated precipitation (APCP) forecasts from the truth and background runs are verified against the

208   rain gauge measurements at national weather stations in the Beijing-Tianjin-Hebei region (Fig. 2).

209   Compared with the rainfall observations (color-filled dots in Fig. 2 e and f), the truth simulation

210   generally captured the southwest-to-northeast orientation and northeastward movement of the observed

211   precipitation in Beijing, although it underpredicted the precipitation in southeastern Hebei (Fig. 2a and

212   b). Conversely, NoDA produced a more west-east oriented rainfall pattern south of Beijing, rather than

213   a southwest-to-northeast band structure. NoDA missed the precipitation in southeastern Hebei (Fig. 2c),

214   whereas it overpredicted the rainfall in western Hebei and areas along Beijing's southern border (Fig.

215   2d). Notably, the NoDA experiment failed to predict the convection in southwestern Beijing during the

216   CI stage (discussed later in Sect. 4.1.2).
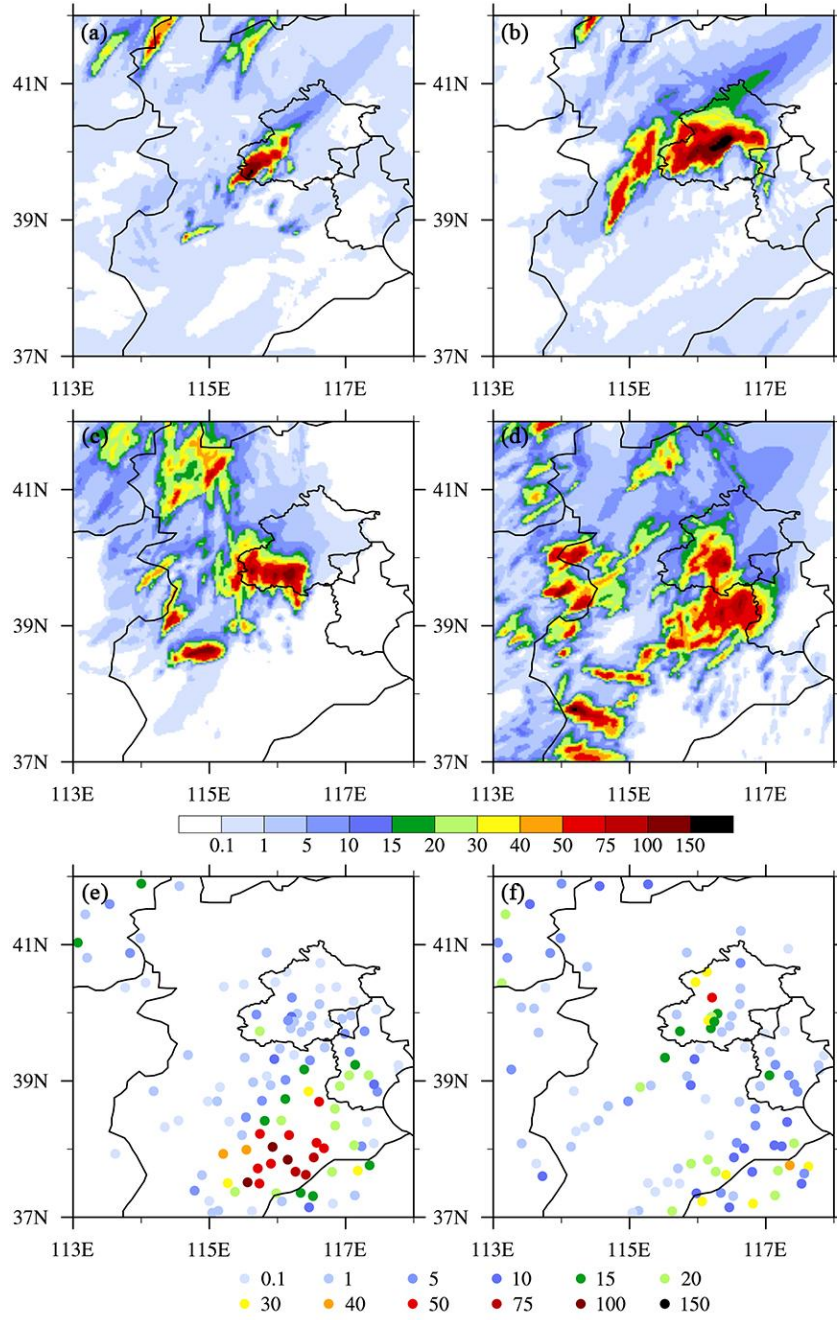
Figure 2. The 6-h accumulated precipitation (APCP) forecasts (mm, shaded) from 2100 UTC 20 July to 0300 UTC 21 July (left), and from 0300 UTC 21 July to 0900 UTC 21 July, 2023 (right) for (a)-(b) Truth, (c)-(d) NoDA experiments, and (e)-(f) the rain gauge measurements at national weather stations.

3.2 Synthetic RWP observations

The real-time Chinese RWP network provides horizontal wind direction, horizontal wind speed, and vertical wind speed at 60-240 m intervals, from the ground surface up to 3-10 km, depending on the operating frequency (Liu et al., 2020). The network comprises three RWP types: high-troposphere,

225   low-troposphere, and boundary layer RWPs, with the majority being boundary layer RWPs operating

226   in the L band. The China Meteorological Administration's data center provides wind profiling products

227   at 6-, 30-, and 60-min intervals for each operational site. To generate synthetic profiles of zonal and

228   meridional wind (u and v) components at operational RWP sites within the simulation domain (30 sites

229   total), truth wind vectors from model grids are interpolated onto each site using the bilinear

230   interpolation method (Fig. 3, blue stars). Additionally, we assume more observations are available at

231   upstream sites near Beijing, specifically along the foothill and ridge of the Taihang Mountains (Fig. 3,

232   red and magenta stars). The spatial locations for the foothill and ridge sites, with a total of 16 sites each,

233   are determined based on the ETOPO1 Global Relief Model, a 1-arc-minute resolution topographic and

234   bathymetric dataset provided by NOAA's National Centers for Environmental Information (Amante

235   and Eakins, 2009). In this study, maximum detection heights of 3, 8, and 12 km, and vertical

236   resolutions of 60 and 120 m have been chosen to mimic the vertical range and resolution of most real

237   RWP data. Synthetic wind profile at each simulated RWP site is assumed to be at the height H, which

238   is defined as follows:

239
$$H(1) = H_{elev} + 500$$
$$H(k) = H(1) + k \times H_{inc}, \quad \text{if } H(k) \le H_{max} \tag{2}$$

240   where H_{elev} is the elevation of the observation site, k is the index number of the vertical level, H_{inc} and

241   H_{max} are specified vertical resolution and maximum detection height, respectively. The units of all

242   height variables are meters. Similar to Zhang et al. (2016), 500 m is selected as the first level of wind

243   profile used for assimilation. The final observations are obtained by adding perturbations to the wind

244   profiles extracted from the truth run. The perturbations are assumed to be normally distributed

245   Gaussian random errors with a mean of zero and a standard deviation of 2 m/s (Hu et al., 2017; Huang

246   et al., 2020; Zhao et al., 2021a).

247   As our focus is to assess the impacts of assimilating wind observations from various RWP

248   network layouts on convective-scale analysis and short-term severe weather prediction, only synthetic

249   RWP data are assimilated in this study, excluding conventional observations such as radiosondes,

250   surface weather stations, and satellite observations. This exclusion simplifies the analysis by isolating

251   the impact of RWPs but may inflate their relative importance (Hoffman and Atlas, 2016).
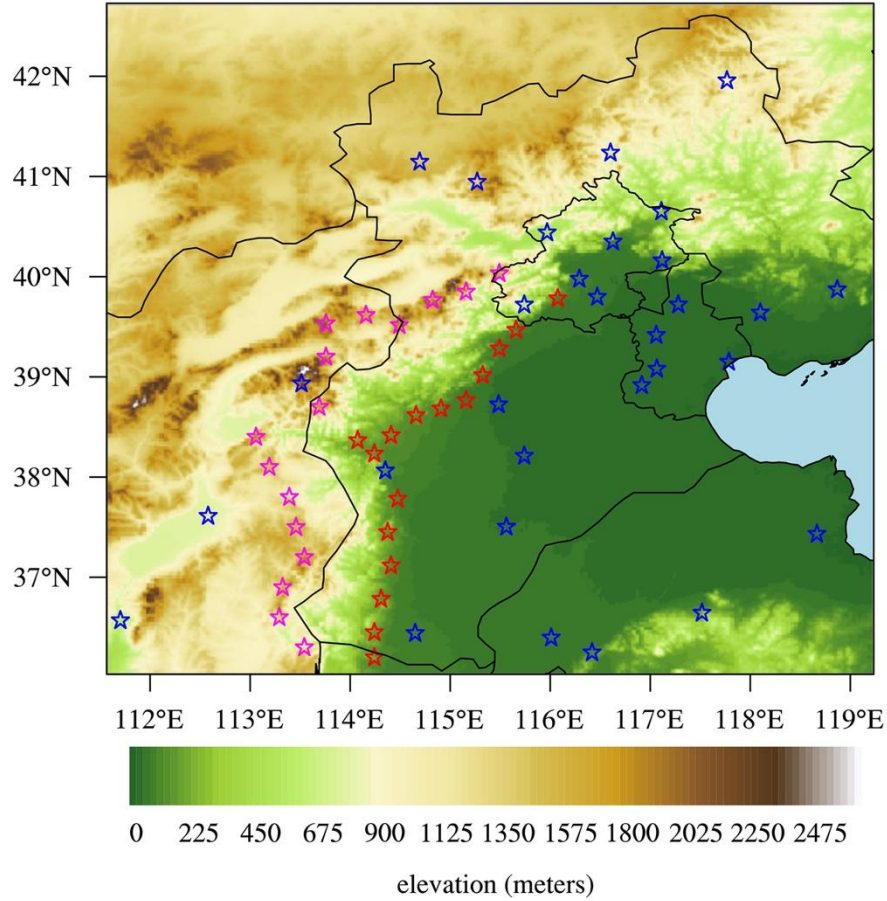
Figure 3. Spatial distribution of the operational RWP network (blue stars), and simulated RWP network along the foothill (red stars) and ridge (magenta stars) of the Taihang Mountains within the simulation domain. The terrain is represented by color shading, and the ocean is shown in light blue.

3.3 Experimental Design

To mimic real-world operations, this OSSE study employs a DA and forecast cycle workflow similar to the Warn-on-Forecast System (WoFS) real-time Spring Forecast Experiment (SFE) runs, that is cycling DA for 9 hours at 15-min intervals (Heinselman et al., 2024; Hu et al., 2020; Jones et al., 2018) (Fig. 4). To minimize data contamination from precipitation, DA cycles are performed before widespread rainfall occurs in the simulation domain, as wind profile accuracy from RWPs can be degraded by falling hydrometeors (Zhang et al., 2017). The model initial and boundary conditions for all DA and forecast experiments are derived from the 12-h GFS forecasts. Unlike the SFE setupa 6-h free forecast in this study is launched every hour starting from the sixth hour of the analysis cycles, rather than from the first hour (Fig. 4). This delayed forecast initiation allows convective systems to develop, as they are typically not yet initiated or developed during the initial hours of assimilation

267   cycles. For comparison, a first-guess background run (NoDA) is conducted by advancing the model

268   forward without assimilating any observations.

269
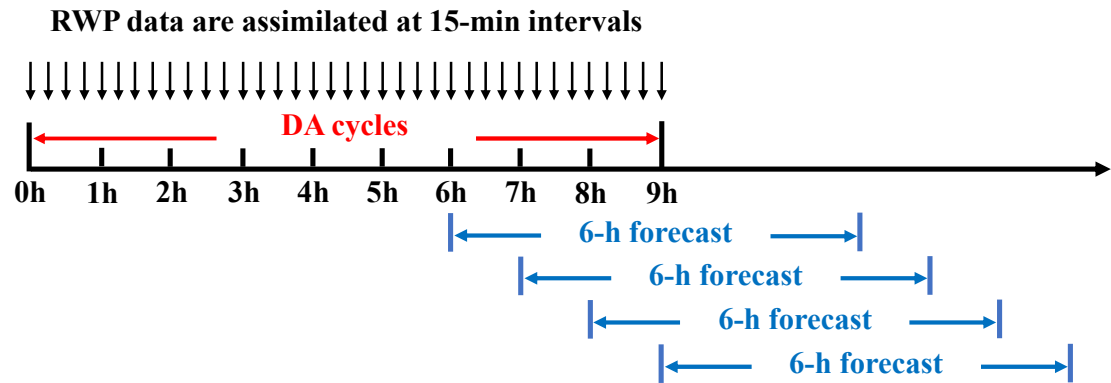
270   **Figure 4.** Illustration of the data assimilation and forecast cycle workflow. A 6-h forecast is launched

271   every hour from the sixth hour to the end of the DA cycles (namely, four separate forecasts).

272   To investigate the impact of simulated foothill and ridge RWP networks on convective-scale

273   NWP, four types of DA experiments are performed (Table 1). These experiments differ in their

274   assimilation of synthetic profiler data from various RWP network spatial layouts. The baseline

275   experiment, CTL, assimilates synthetic observations from the operational RWP network with a vertical

276   resolution of 60 m (from 500 m to 8 km height), serving as a benchmark for comparison. This vertical

277   resolution represents a best-case scenario for RWP capabilities.

278   **Table 1**. List of the DA sensitivity experiments based on various spatial layout schemes of radar wind

279   profiler (RWP) network over the Beijing-Tianjin-Hebei region.

Experiment	Operational	Foothill	Ridge	Maximum height (km)	Vertical resolution (m)
CTL	✓			8	60
FH	✓	✓		8	60
RD	✓		✓	8	60
FH_RD	✓	✓	✓	8	60
FH_RD_V120	✓	✓	✓	8	120
FH_RD_H3	✓	✓	✓	3	60
FH_RD_H12	✓	✓	✓	12	60

280   CTL: control DA experiment;   FH: foothill;   RD: ridge

281   The second and third types of experiments assimilate the simulated foothill and ridge RWPs,

282   respectively, in conjunction with data from operational sites (referred to as FH and RD). The fourth

283   type of experiment FH_RD is performed by assimilating the operational, foothill, and ridge profilers

284   with the same vertical resolution and maximum detection height as before. Additionally, three

285   sensitivity experiments FH_RD_V120, FH_RD_H3, FH_RD_H12 are designed to assess the influence

286   of assimilating RWP data with different vertical resolution (120 m) and maximum detection heights (3

287   km, 12 km) on the analyses and forecasts, to address the potential usage of real-time data from RWPs

288   operating at different frequencies.

289   In all DA experiments, the background errors for zonal and meridional wind components are

290   specified as 3–6 m/s, gradually increasing with altitude from the surface to 20 km above ground level

291   (AGL). The observation error is set to 3 m/s, based on sensitivity tests within the 2–6 m/s range and

292   consistent with previous studies (Hu et al., 2017; Huo et al., 2023; Wang et al., 2022; Zhang et al.,

293   2016). In the minimization process two outer loops are adopted, each with a prescribed horizontal and

294   vertical correlation scale for the recursive filter used in the program (Gao et al., 2004; Purser et al.,

295   2003). Following previous studies (Wang et al., 2022; Zhao et al., 2022). The horizontal correlation

296   scale lengths are set to be 50 km in the first loop and 20 km in the second loop, while the corresponding

297   vertical correlation lengths are 5 and 2 grid points, respectively.

298   **3.4 Evaluation metrics**

299   This study examines the impact of RWP DA on wind analyses and forecasts during a southwest

300   (SW)-type heavy rainfall event on 21 July 2023. To obtain an overall insight into the impact of RWP

301   DA on wind analyses and forecasts, time series and probability density distributions, as well as vertical

302   profiles of root-mean-square errors (RMSEs) for wind components during the DA cycles and 6-h free

303   forecasts are calculated for each type of assimilation experiment. Additionally, subjective diagnostic

304   analyses of wind vectors improved by assimilation of RWPs are also discussed in more detail. To

305   investigate the impact on short-term forecasts, both qualitative and quantitative assessments of radar

306   reflectivity and accumulated precipitation forecasts are conducted against the truth run. To evaluate the

307   performance quantitatively, the neighborhood-based equitable threat score (ETS, Clark et al., 2010) is

308   calculated using a neighborhood radius of 12-km for different thresholds of composite reflectivity

309   (CREF) and hourly precipitation (HPRCP). Using the same neighborhood radius and thresholds,

310 contingency-table based metrics including the probability of detection (POD), false alarm ratio (FAR),

311 success ratio (SR), frequency bias (BIAS), and critical success index (CSI) are also calculated to

312 quantify the CREF and HPRCP forecasts. To account for case-to-case variability, two additional

313 SW-type heavy rainfall events (28 June and 12 July 2023) are examined. Finally, score metrics are

314 aggregated from each initialization hour (sixth hour to end of the DA cycles) across three cases,

315 ensuring a fair and consistent measure of forecast skill.

316 **4 Results and discussion**

317 **4.1 21 July 2023 case**

318 **4.1.1 The impact on wind fields**

319   The first question we attempt to answer is how the spatial distribution of RWP sites should be

320 planned to optimize the accuracy of short-range convection-allowing NWP system (Potvin and Flora,

321 2015). The influence of assimilating RWP data from different networks, as described in Sect. 3.3, on

322 wind analysis and forecast can be straightforwardly assessed by examining the RMSEs of wind

323 components during the 9-h assimilation cycles and 6-h free forecasts. For clarity, the time series and

324 probability density distribution (PDF) of the wind RMSEs from the CTL, FH, RD, and FH_RD

325 experiments are compared in Fig. 5. The statistics are computed against the truth run at all model levels

326 within the simulation domain shown in Fig. 3. Overall, the RMSEs of wind analyses from all DA

327 experiments during the analysis cycling decrease over the first six hours and then gradually increase

328 afterward, exhibiting an evident staircase pattern (Fig. 5a and c), indicating that the wind field is

329 modified by the NSSL3DVAR system towards the truth in each analysis cycle. A comparison among

330 all DA experiments reveals that the FH_RD experiment yields the smallest wind errors, followed by

331 RD, then FH, with CTL exhibiting the largest errors. This likely occurs because (a) FH_RD assimilates

332 the largest amount of wind observations, while CTL assimilates the fewest, and (b) the uncertainties of

333   wind field in the background field are larger in mountainous regions than flatlands (this issue will be

334   discussed in detail later in this section). The superiority of FH_RD, RD, and FH over the CTL

335   experiment persists during the subsequent 6-h free forecasts, highlighting the impact of wind profile

336   observations gathered from ridge and foothill networks. It is also noted that the difference in the

337   meridional wind among FH, RD, and FH_RD is more pronounced than that of the zonal wind, which

338   can be related to the varying degree of improvement in the southerly jet intensity. Generally, the PDF

339   figures show that the distributions of wind analyses are skewed towards smaller error values compared

340   to those of forecasts, with the wind forecasts exhibiting a heavy tail towards larger error values (Fig. 5b

341   and d). For example, the analysis errors for the v variable tend to cluster around 1.6–2.6 m/s, while the

342   PDFs of forecast errors show peaks near 2.0–3.4 m/s. The patterns in distributions from different

343   assimilation experiments align with the results observed in the time series analysis.
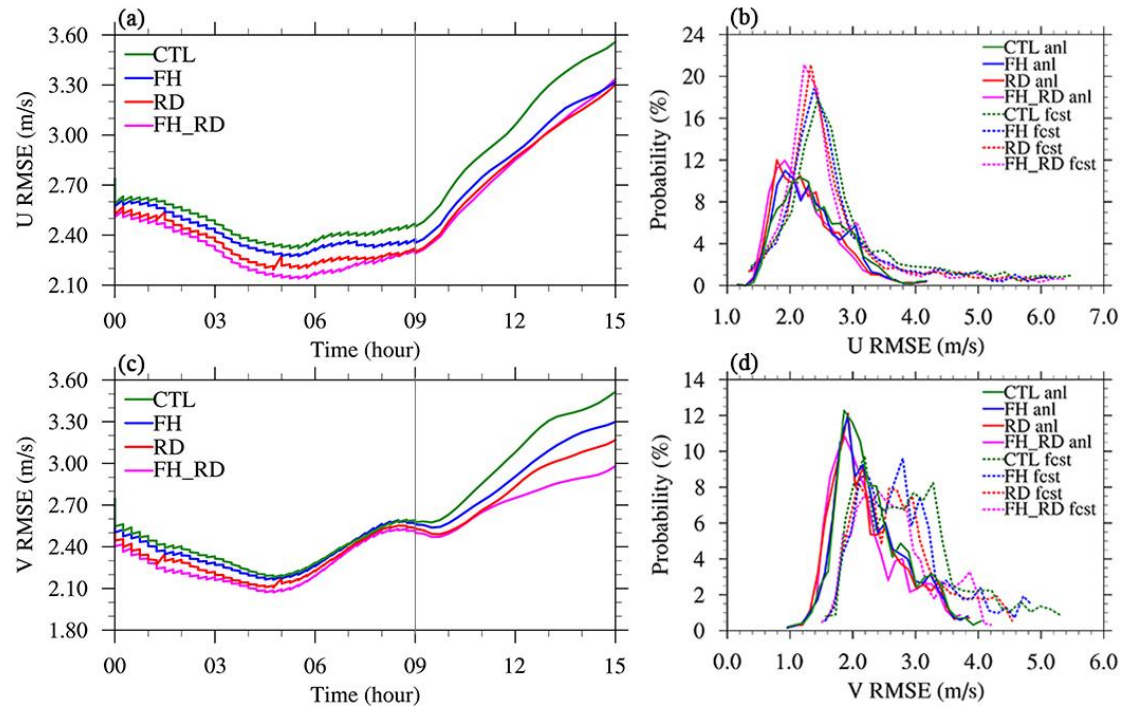
345   **Figure 5.** Time series of root-mean-square errors (RMSEs) for (a) u (m s^{-1}), and (c) v (m s^{-1}) analyses

346   and forecasts from the CTL (green), FH (blue), RD (red), and FH_RD (magenta) experiments. The thin

347   grey line separates analysis cycling and 6-h free forecasts. Probability density distribution (PDF) of

348   RMSEs for (b) u (m s^{-1}), and (d) v (m s^{-1}) analyses (solid) and forecasts (dashed) from four

349   experiments.

350   To assess the impact of the DA experiments at different altitudes, Fig. 6 presents the vertical

351   profiles of domain-averaged RMSEs of wind analyses at the end of the assimilation cycles. Compared

352   to the NoDA experiment, the assimilation of RWPs generally has a positive effect on the wind field

353   throughout the troposphere. The CTL experiment slightly reduces the wind errors, specifically in the

354   layer from 850 to 600 hPa for the *u* component and from 500 to 300 hPa for both components. It is seen

355   that the DA experiments assimilating ridge and foothill RWPs generally outperform CTL. For the *u*

356   wind component, the RD experiment has a comparable RMSE profile to FH below 550 hPa but results

357   in a much smaller error above (Fig. 6a). In the analysis of the *v* wind, RD consistently performs better

358   than FH, except for the layer from 260 to 160 hPa (Fig. 6b). Notably, FH_RD results in the smallest

359   wind errors across most levels, aligning with the previously observed error trends over time.
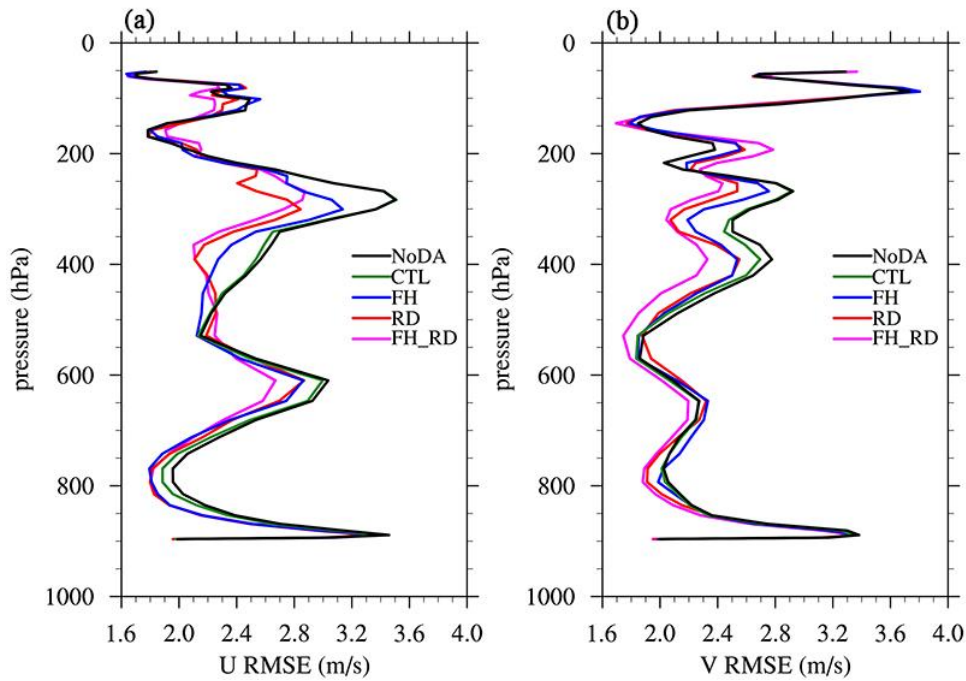
361 **Figure 6.** Vertical profiles of domain-averaged RMSEs for (a) u (m s^{-1}), and (b) v (m s^{-1}) analyses at

362 2100 UTC 20 July 2023 (end of analysis cycling) from the NoDA (black), CTL (green), FH (blue), RD

363 (red), and FH_RD (magenta) experiments.

364   To examine how the RWP DA adjusts the mesoscale airflow, we present the 700-hPa wind

365   vectors and wind speeds from all experiments as an illustration of the model's dynamic conditions (Fig.

366   7). For clarity, Fig. 7b-f compare the differences in wind vectors and wind speeds between the DA

367   experiments and the corresponding field from the truth run. These differences, considered as wind

368   errors, help evaluate how assimilating RWPs from different observation networks adjusts the wind field.

369   The red (blue) color represents positive (negative) wind speed bias compared to the truth. In the NoDA

370   experiment, there is a notable southeasterly wind bias in Beijing and the mountainous regions to its

371   west, characterized by excessively high wind speeds. Conversely, the true simulation reveals a strong

372   southwesterly flow (Fig. 7b). Meanwhile, the southwest wind is remarkably weaker in southwestern

373   Hebei (at the foothills of the Taihang Mountains), and the westerly wind in the upstream Taihang

374   Mountains region is also underestimated. The CTL experiment significantly reduces the easterly wind

375   bias in Beijing and its surrounding areas while enhancing the southwesterly winds in Hebei (Fig. 7c).

376   However, unignorable wind errors persist upstream of Beijing, particularly along the mountainous

377   regions, due to the absence of operational wind profiler sites. The FH experiment produces wind

378   adjustments similar to those in CTL but further reduces wind errors in the plains of Hebei by

379   assimilating observations from foothill sites (Fig. 7d). Conversely, with the assimilation of RWP data

380   from the ridge network, both RD and FH_RD significantly reduce positive wind speed errors upstream

381   of Beijing along the mountains, which is crucial for convection initiation (CI) near the boundary

382   between Hebei and southwestern Beijing (Fig. 7e and f). While the southwest winds in southwestern

383   Hebei remain slightly weaker in RD, FH_RD addresses this by assimilating ridge RWPs alongside

384   foothill data. However, all DA experiments still show negative wind speed errors and

385   northwesterly/northeasterly wind direction errors near the border of Shanxi, Hebei, and Inner Mongolia,

386   with errors even larger than those in NoDA. This is mainly due to the lack of RWP observations in this

387   tri-provincial border area. As a result, the influence of ridge RWP data may propagate northward into

388   this region by the RD and FH_RD experiments, significantly reducing positive errors upstream of

389   Beijing along the mountains but increasing negative errors in this area.

390
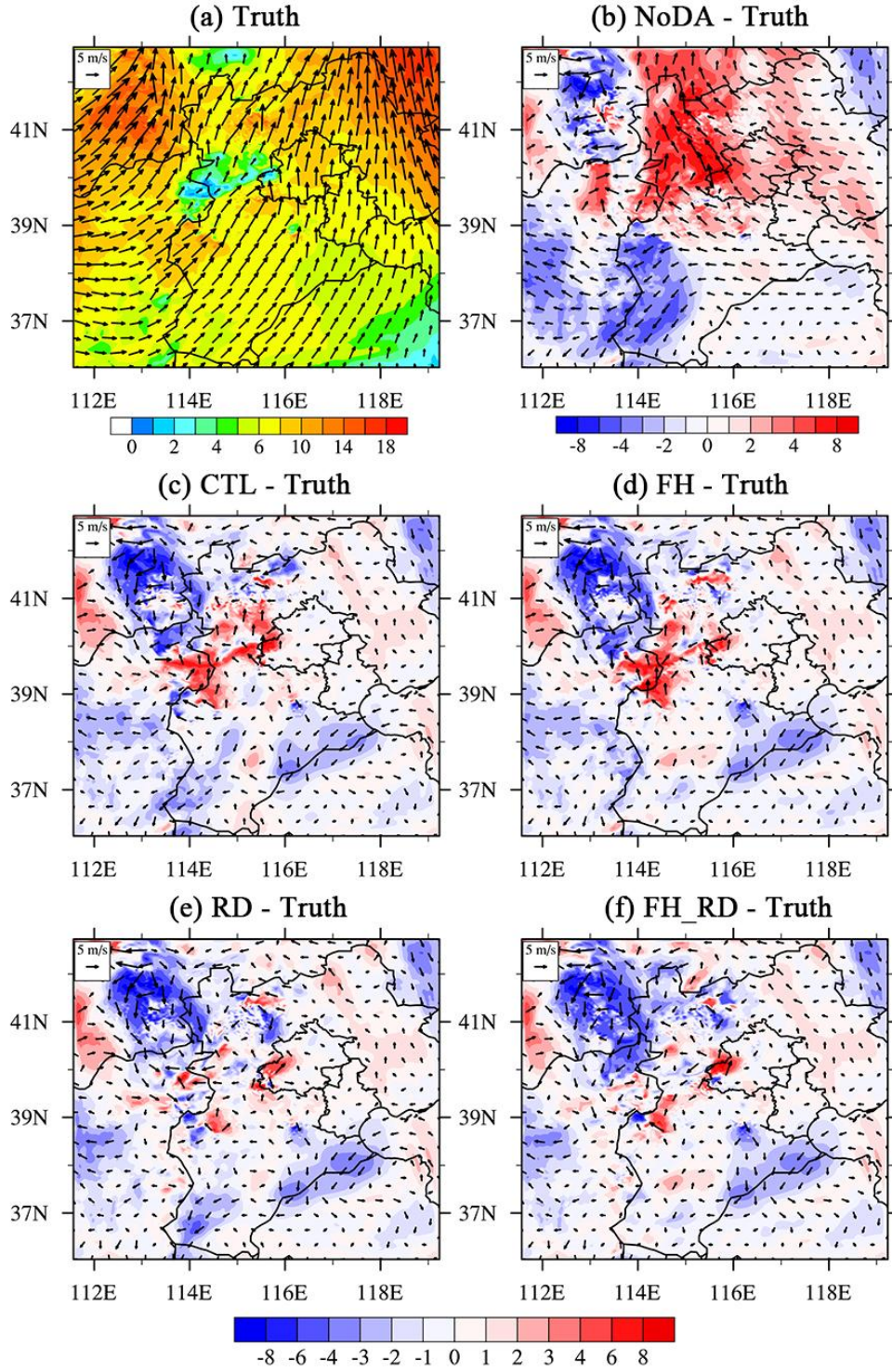
Figure 7. (a) 700-hPa wind (vectors) with wind speed (m s⁻¹, color shaded) from the truth run, and

differences between the 700-hPa winds from (b) NoDA, (c) CTL, (d) RD, (e) FH, and (f) FH_RD

experiments and the truth run at 2100 UTC 20 July 2023 (end of analysis cycling). The red (blue) color

represents positive (negative) wind speed bias compared to the truth.

4.1.2 The impact on reflectivity and precipitation forecasts

The analysis, along with the 3- and 6-h forecasts of composite reflectivity from all experiments, is compared to the truth run in Fig. 8 and 9. In the southwest of Beijing, a convective system initiates and develops. As it merges with scattered storms originating in western Hebei near the foothills of the Taihang Mountains, the system intensifies rapidly. Eventually the convection becomes a southwest-northeast oriented mesoscale system across the western and central parts of Beijing (Fig. 8a-c). At the initial stage, the NoDA experiment underestimates convection in Beijing and Hebei (Fig. 8d), but in the 6-h forecast, NoDA overpredicts the storm coverage and intensity in Beijing and produces excessive spurious convection in western and northern Hebei (Fig. 8d-f). At analysis time, all DA experiments show improvement in the location and shape of the convective system in southwestern Beijing, and FH_RD produces the strongest reflectivity analysis (Fig. 8g, 9a, 9d, and 9g). This implies that the assimilation of RWP data can improve CI timing and location by capturing the mesoscale flow features in the pre-storm environment (Fig. 7). The RWP DA also helps alleviate storm displacement and intensity errors and suppress spurious cells in subsequent forecasts, owing to a better representation of the storm environment. Although CTL correctly analyzes the CI near the observed location, its analysis and 3-h lead-time reflectivity forecast show that the storm intensity in Beijing is still weaker than the truth simulation, especially over western and central Beijing (Fig. 8g-i). The FH experiment produces stronger storms with a larger coverage area in Beijing compared to the CTL experiment, although the storm intensity remains slightly underestimated; however, spurious echoes to the west of Beijing remain evident in the 6-h forecast (Fig. 9a-c). With the assimilation of ridge RWP data, the RD and FH_RD experiments further strengthen the CI process and improve the storm pattern and development. A comparison among all experiments reveals that FH_RD demonstrates overwhelming superiority over the other three DA experiments in terms of areal coverage, storm mode, and storm orientation (Fig. 9g-i).

419
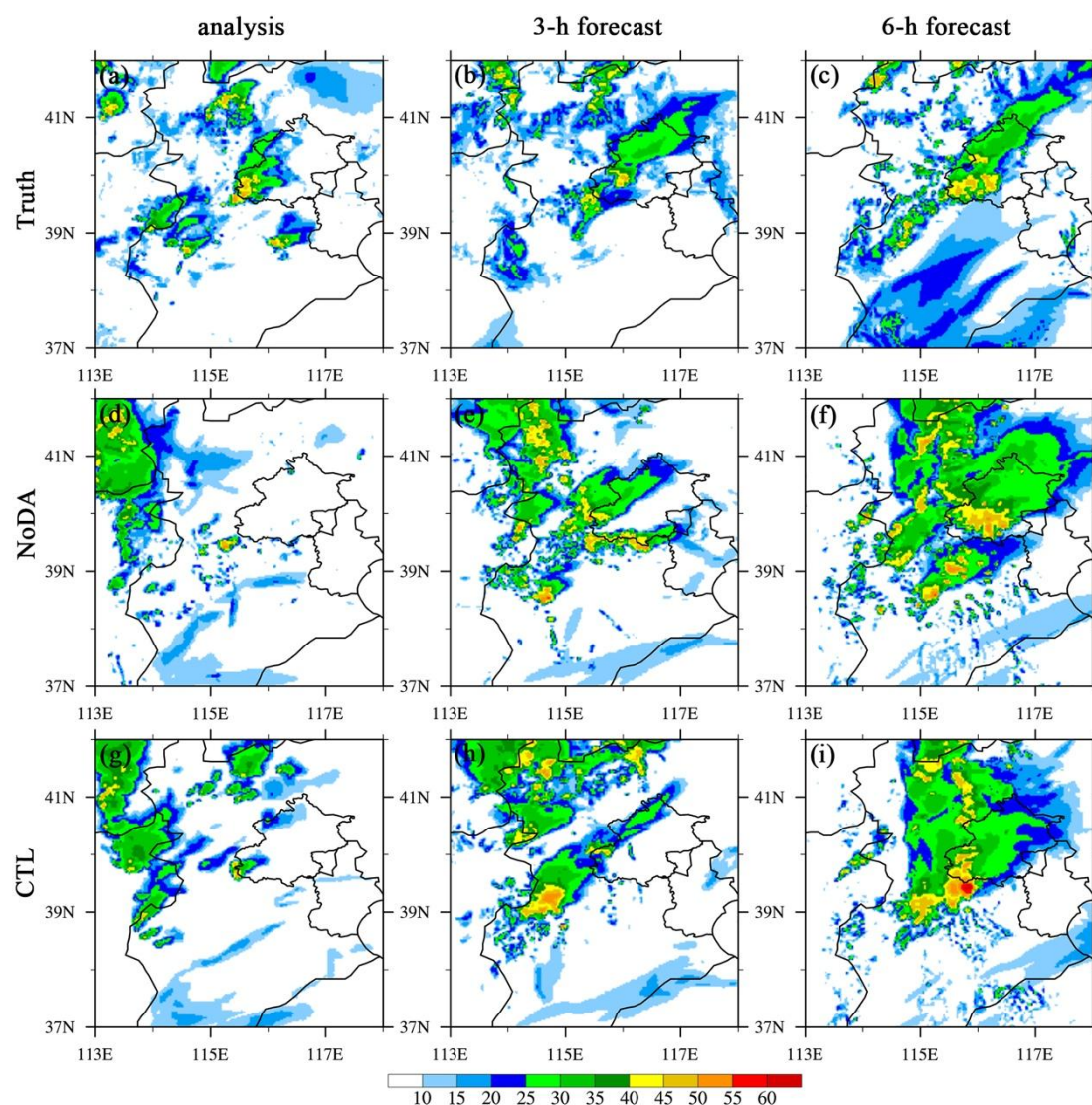
Figure 8. The composite reflectivity (dBZ, shaded) for (left) analysis, (middle) 3-h forecast, and (right)

6-h forecast from (a)–(c) truth simulation, (d)–(f) NoDA, and (g)–(i) CTL experiments initialized at

2100 UTC 20 July 2023.
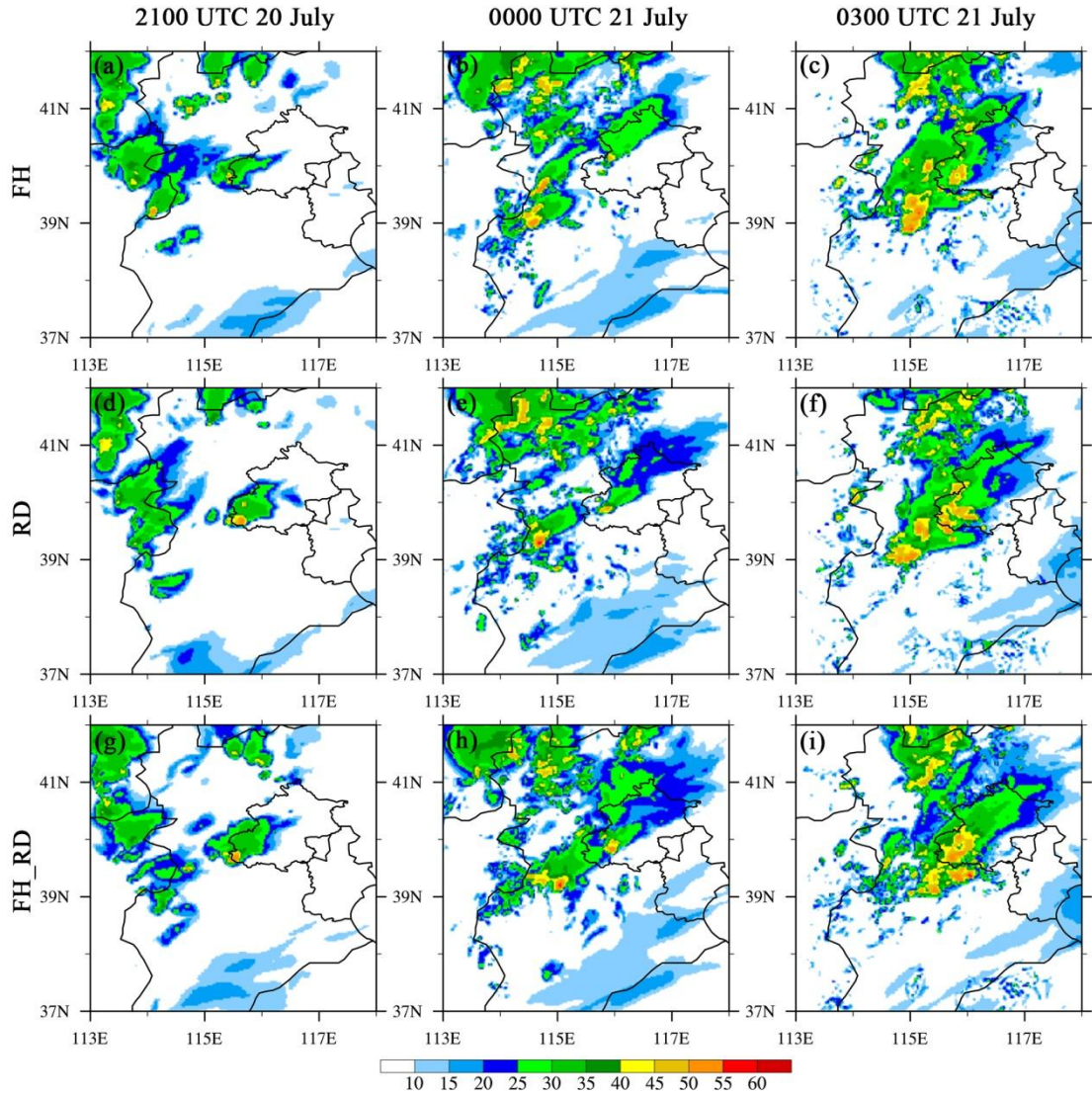
Figure 9. Same as in Fig. 8, but for the composite reflectivity (dBZ, shaded) from (a)–(c) FH, (d)–(f) RD, and (g)–(i) FH_RD experiments.

Concerning precipitation, the 1-, 3-, and 6-h accumulated precipitation (APCP) forecasts exhibit similar behavior to the reflectivity results in terms of rainfall location, onset time, and amount (Fig. 10 and 11). As discussed above, all assimilation experiments predict the initial precipitation area and intensity in the southwest of Beijing more accurately than NoDA, leading to improvements in subsequent APCP forecasts in this area. For example, assimilating ridge and foothill RWPs corrects the weaker biases associated with this storm in the 1- and 3-h forecasts (Fig. 11a-b, d-e, g-h). Meanwhile, the more west-east oriented heavy rainfall occurring over the south of Beijing in the 6-h forecast of NoDA is revised by the assimilation experiments, shifting to a southwest-northeast orientation that is closer to the truth simulation. Although the areal coverage of rainfall in the 1-h forecast is better captured by CTL compared to NoDA, CTL still tends to underpredict the precipitation amount in

436 southwestern Beijing, while overestimation is commonly observed in parts of the mountainous areas to

437 the southwest of Beijing (Fig. 10g-i). One potential factor contributing to the overpredicted rainfall in

438 the mountainous areas to the southwest of Beijing is the CTL experiment's reduction of positive wind

439 errors in Beijing, while higher wind speeds (compared to the truth) persist along the upstream

440 mountains. It is due to the absence of operational wind profiler sites. The stronger southwesterly winds

441 of the CTL experiment enhance moisture transport and convergence in the upstream mountains, leading

442 to overestimated rainfall in those areas and underpredicted precipitation over Beijing. Both RD and

443 FH_RD experiments yield a smaller areal coverage of precipitation at the same region, and they also

444 better capture the southwest-northeast orientation of the rainband in southwestern Beijing (Fig. 11d-i),

445 as the large wind errors in the upstream mountains are remarkably reduce by assimilating RWP data

446 from the ridge network (Fig. 7e and f). As expected, the APCP forecasts from FH_RD align well with

447 the true rainfall forecasts in terms of placement, orientation, and amount (Fig. 11g-i vs. 10a-c).

448
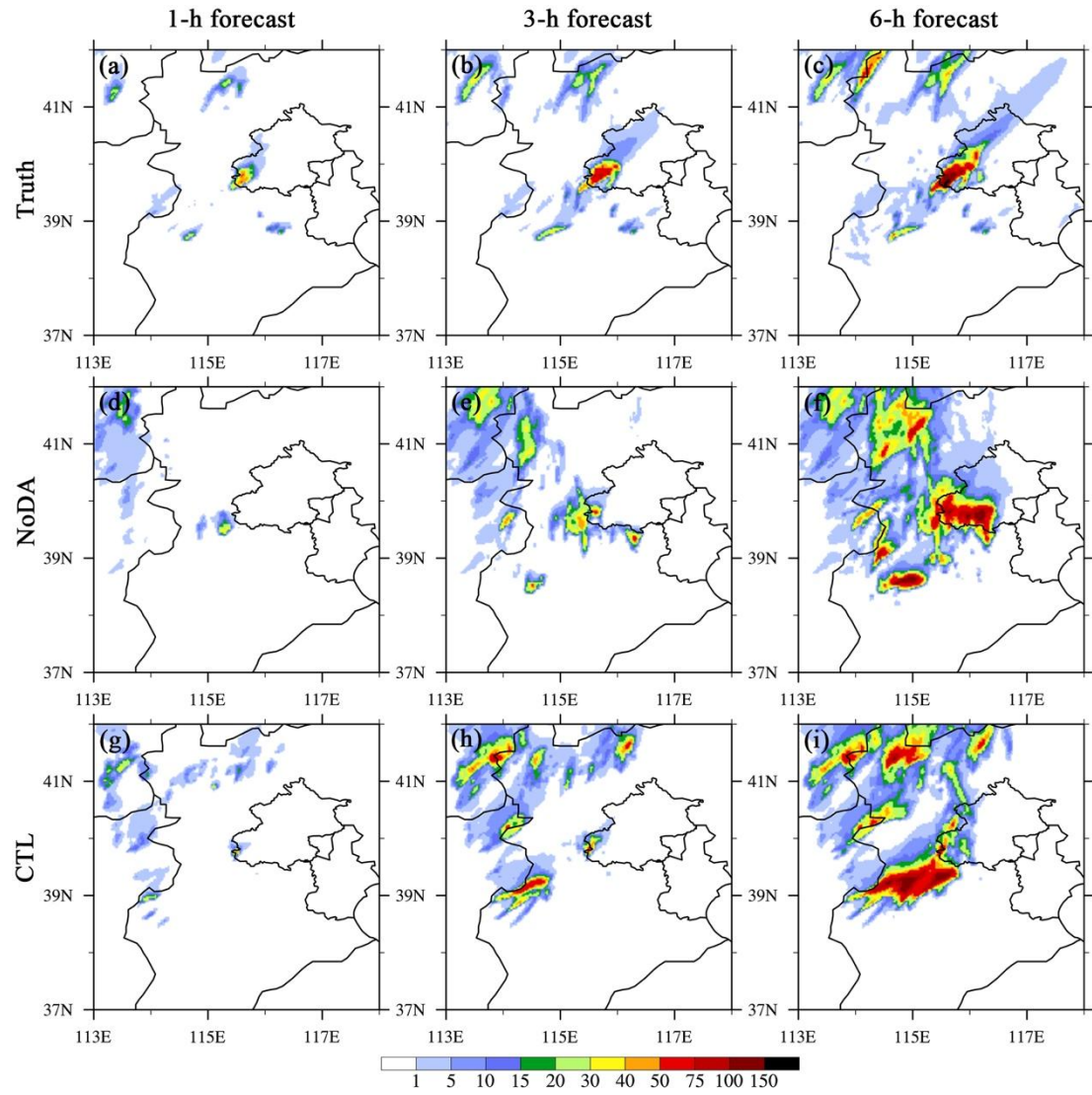
Figure 10. The accumulated precipitation (APCP) forecasts (mm, shaded) for (a)-(c) Truth, (d)-(f)

NoDA, and (g)-(i) CTL experiments initialized at 2100 UTC 20 July 2023. The (left) 1-, (middle) 3-,

and (right) 6-h forecasts are shown.
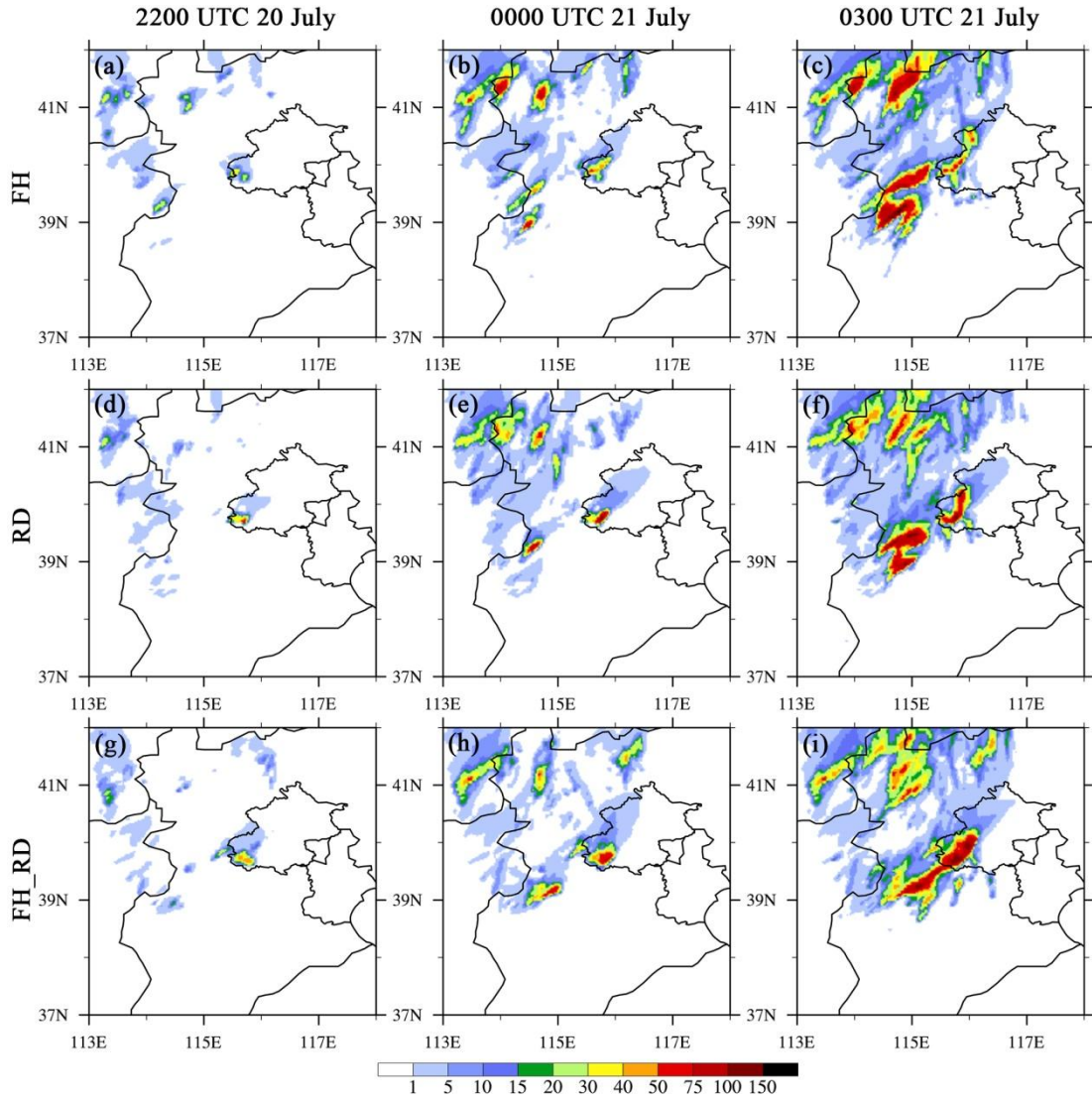
Figure 11. Same as in Fig. 10, but for the APCP forecasts (mm, shaded) from (a)–(c) FH, (d)–(f) RD, and (g)–(i) FH_RD experiments.

To quantify the performance of the reflectivity and precipitation forecasts by assimilating RWP data from different observation networks, categorical performance diagrams and neighborhood-based ETS are calculated and aggregated over four 6-h free forecasts. These forecasts are launched hourly from the sixth hour to the end of the analysis cycle. All score metrics are computed for a neighborhood radius of 12 km. The ETS for composite reflectivity is calculated every 15 minutes, while for APCP, it is calculated hourly. In the performance diagrams, values of POD, SR (1 – FAR), and CSI closer to unity indicate higher forecast skill, with the perfect forecast located at the upper-right corner of the diagram. A BIAS value greater (less) than unity indicates overprediction (underprediction). Because of decreased PODs along with increased FARs, most experiments show a slight decline in forecast scores when the composite reflectivity threshold increases from 20 to 40 dBZ (Fig. 12). Overall, all DA

465   experiments consistently outperform NoDA at all thresholds, exhibiting higher POD, SR, CSI, and ETS

466   values, except for the CTL (FH and FH_RD) experiment during the 0-4 h (4-5 h) forecast period at the

467   threshold of 40 dBZ. Among them, the FH_RD, RD, and FH experiments show overwhelming

468   superiority over CTL for the 0-4 h reflectivity forecasts in terms of ETS, POD, SR and CSI values at all

469   thresholds. For the 20- and 30-dBZ thresholds, it is evident that FH_RD produces the highest ETS,

470   POD, SR, and CSI scores during the 0-3 h forecast period, the improvement in BIAS values was

471   minimal (Fig. 12a-d). However, for 40 dBZ, the RD experiment achives slightly higher ETS, POD, SR,

472   and CSI scores than FH_RD does at most forecast lead times (Fig. 12e and f). It is also worth noting

473   that, for 20- and 30-dBZ thresholds, FH produces higher ETS , POD, and CSI scores than RD does

474   before the 2-h forecast lead time, while RD exhibits better forecast skill thereafter (Fig. 12a-d). This

475   suggests that assimilating RWP data from the foothill network is more effective in the first two hours,

476   while ridge site observations have a more pronounced positive impact between 2 and 6 hours.

477   Additionally, the period during which FH outperforms RD shortens when the threshold increases from

478   20 to 40 dBZ.

Figure 12. Aggregate score metrics of 0-6 h composite reflectivity (CREF) forecasts aggregated from each initialization hour from the sixth hour to the end of the DA cycles for case 1 for the NoDA (black), CTL (green), FH (blue), RD (red), and FH_RD (magenta) experiments. (left) The performance diagrams, and (right) the equitable threat score (ETS) for (a)–(b) 20 dBZ, (c)–(d) 30 dBZ, and (e)–(f) 40 dBZ thresholds, respectively. Results are shown for a neighborhood radius of 12-km. The numbers within the colored dots in the performance diagrams denote the forecast hour (i.e. 0-, 3- and 6-h forecasts).

487   A similar trend and behavior are observed in the performance diagrams and ETS figures for the

488   HPRCP forecast, highlighting the superior performance of the RD and FH_RD experiments (Fig. 13).

489   In general, lower score metrics are obtained when a higher threshold for precipitation forecasts is

490   evaluated, likely resulting from a lower frequency of occurrence for heavy precipitation. As seen in the

491   CREF forecast, the FH_RD, RD, and FH experiments show more skillful precipitation forecasts than

492   CTL does. In terms of the 2.5-mm precipitation forecast, FH_RD generally achieves the highest POD,

493   SR, CSI, and ETS, along with the smallest BIAS, with RD exhibiting slightly inferior performance (Fig.

494   13a and b). For the 5-mm threshold, FH generates the highest POD and ETS in the first 3 hours,

495   whereas RD delivers the lowest FAR and largest ETS in the subsequent 3-h forecasts (Fig. 13c and d).

496   The RD experiment outperforms all the other experiments in the 1-, 3-, and 4-h forecasts at the

497   threshold of 10 mm (Fig. 13e and f). One possible reason for the inferior performance of FH_RD and

498   FH compared to RD at higher thresholds is that FH_RD exhibits a slight southward displacement error

499   for the 1-3 h heavier precipitation (>10 mm) forecasts in southwestern Beijing compared to the truth

500   simulation, while the precipitation in the FH experiment is located further north (Fig. 11a-b, 11g-h vs.

501   Fig. 10a-b). This may lead to larger penalties in the calculation of POD and ETS, resulting in lower

502   scores.
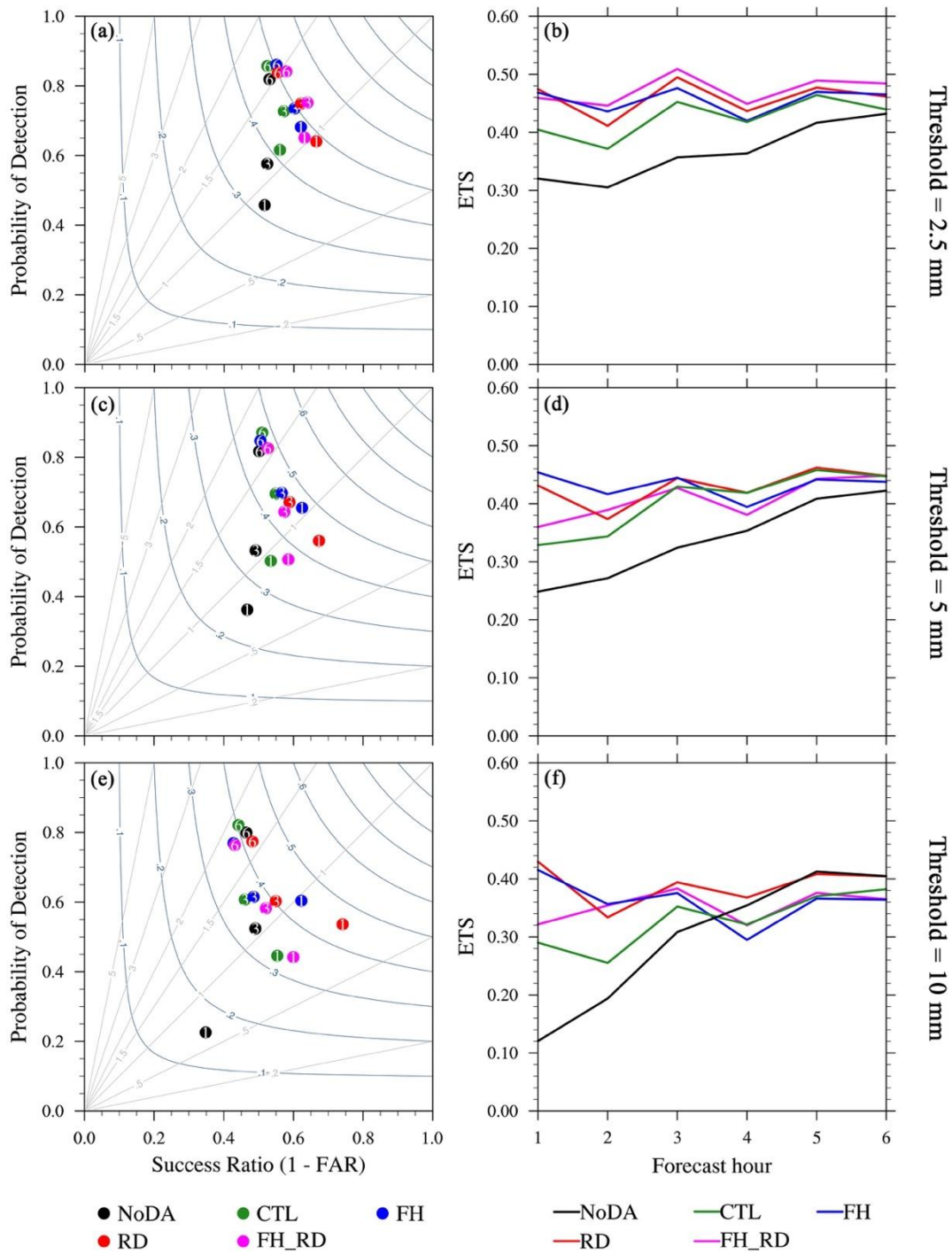
Figure 13. Same as in Fig. 12, but for 1-6 h hourly precipitation amount (HPRCP) forecasts for case 1 at thresholds of 2.5 mm (1st row), 5 mm (2nd row), and 10 mm (3rd row), respectively.

4.1.3 Sensitivity to vertical resolution and detection height

Given the encouraging preliminary results from the FH_RD experiment, ETS figures of CREF and HPRCP forecasts from three additional sensitivity experiment—FH_RD_V120, FH_RD_H3, and FH_RD_H12—are compared to examine the relative impact of different vertical resolutions and

510   maximum detection heights on the analyses and forecasts (Fig. 14). For reflectivity forecasts at

511   thresholds of 20-40 dBZ, the 0-3 h ETSs of FH_RD and FH_RD_H12 are comparable. However, the

512   FH_RD_H12 experiment achieves higher forecast scores after 3 hours, highlighting the benefit of a

513   higher detection height (Fig. 14a-c). Conversely, the FH_RD_H3 experiment (with the lowest detection

514   height of 3 km) shows the smallest ETS values at 20 and 30 dBZ, while FH_RD_V120 (with a lower

515   vertical resolution of 120 m) demonstrates the poorest forecast skill at 40 dBZ. Consistent with the

516   CREF forecast, both FH_RD and FH_RD_H12 show more skillful HPRCP forecasts than

517   FH_RD_V120 and FH_RD_H3. However, the ETSs of FH_RD are higher than those of FH_RD_H12

518   at most forecast lead times, which differs from the reflectivity results. Additionally, FH_RD_H3

519   produces the lowest ETS values throughout the 0–6 h forecasts at thresholds of 2.5–10 mm. Generally,

520   the higher the maximum detection height of RWPs and the denser the vertical distribution of

521   observations, the more significant the positive impact of RWP DA in terms of ETS. Moreover, a

522   maximum detection height of 8 km seems to be a reasonable and effective choice, while the reduction

523   of vertical resolution from 60 m to 120 m has less impact compared to the effect of decreasing the

524   detection altitude to 3 km.

525
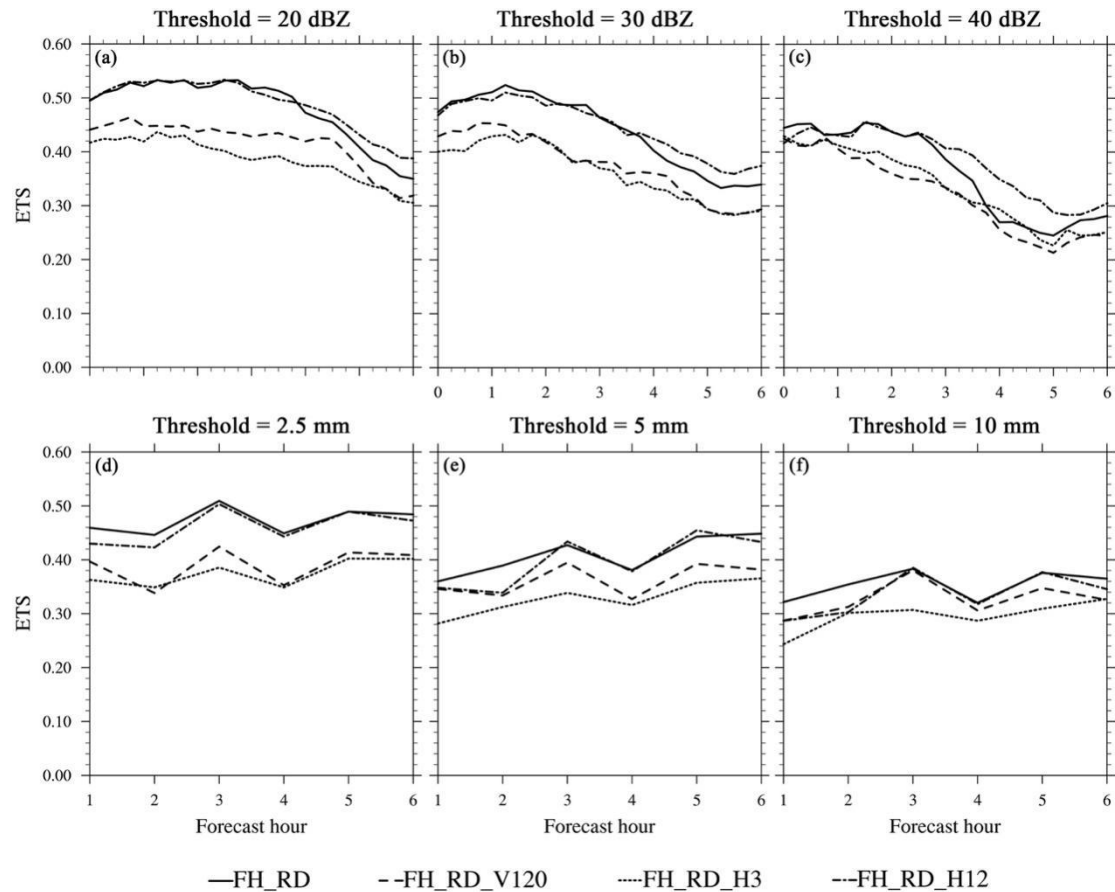
Figure 14. Equitable threat score (ETS) for 0-6 h CREF forecasts from the FH_RD (solid), FH_RD_V120 (dashed), FH_RD_H3 (dotted), and FH_RD_H12 (dashdot) experiments for case 1 at thresholds of (a) 20, (b) 30, and (c) 40 dBZ, respectively. (d–f) Same as in (a–c), but for 1-6 h HPRCP forecasts from each experiment at thresholds of (d) 2.5, (e) 5, and (f) 10 mm, respectively.

4.2 Aggregate forecast performance

Considering the variations in weather scenarios and storm environments across cases, we also examined two additional SW-type heavy rainfall events that occurred over the Beijing-Tianjin-Hebei region on 28 June and 12 July 2023 to evaluate the impact of RWPs observed from different spatial layouts on short-term forecasts. Despite the presence of a southwesterly jet stream in all three cases, they produced distinct storm modes under different weather conditions. To delve deeper into the verification metrics from the three cases, we present performance diagrams of CREF and HPRCP forecasts from the FH_RD experiment as the best assimilation experiment (Fig. 15). The results from the NoDA experiment are also shown to provide a clear picture of how RWP observations improve the short-term forecasts across different cases. For both the NoDA and FH_RD experiments, the forecast skills generally exhibit lower score metrics and more variability at higher thresholds. Overall, for different cases, the FH_RD experiment shows higher POD, CSI, and SAR values compared to the NoDA experiment, with more significant improvements observed in the first 3 hours. Most of the BIAS values for FH_RD are smaller than those for the NoDA experiment. Except for 28 June 2023, the BIAS values of FH_RD fall within a reasonable range of 0.8–1.7 for reflectivity precipitation, indicating overall good forecast performance. It is noted that some of the forecast scores do not decrease monotonically with increasing forecast lead time. For example, in the case 12 July 2023, smaller BIAS and FAR values are obtained for the 3- and 6-h reflectivity and precipitation forecasts, along with higher CSI. This occurs due to several factors: (a) initial scattered convection develops into a larger-scale west-east oriented system covering all of Beijing and central-northern Hebei at later times in this case, which models usually capture better; (b) errors in the timing and location of CI become less significant as convection evolves and forms clearer structures; and (c) for the free forecasts initialized from the first few hours, convection may not have started until the final forecast hour. CREF forecasts from FH_RD for the case 28 June 2023 show the best performance in terms of high POD, SR, and CSI. Meanwhile, persistent underprediction throughout the 1–6 h precipitation forecasts at all

555 thresholds from this case can mostly be traced back to the difficulty in forecasting small-scale,

556 short-lived, and relatively weak precipitation events. This phenomenon is more pronounced in the

557 NoDA experiment, manifested by extremely low POD and CSI values.

558
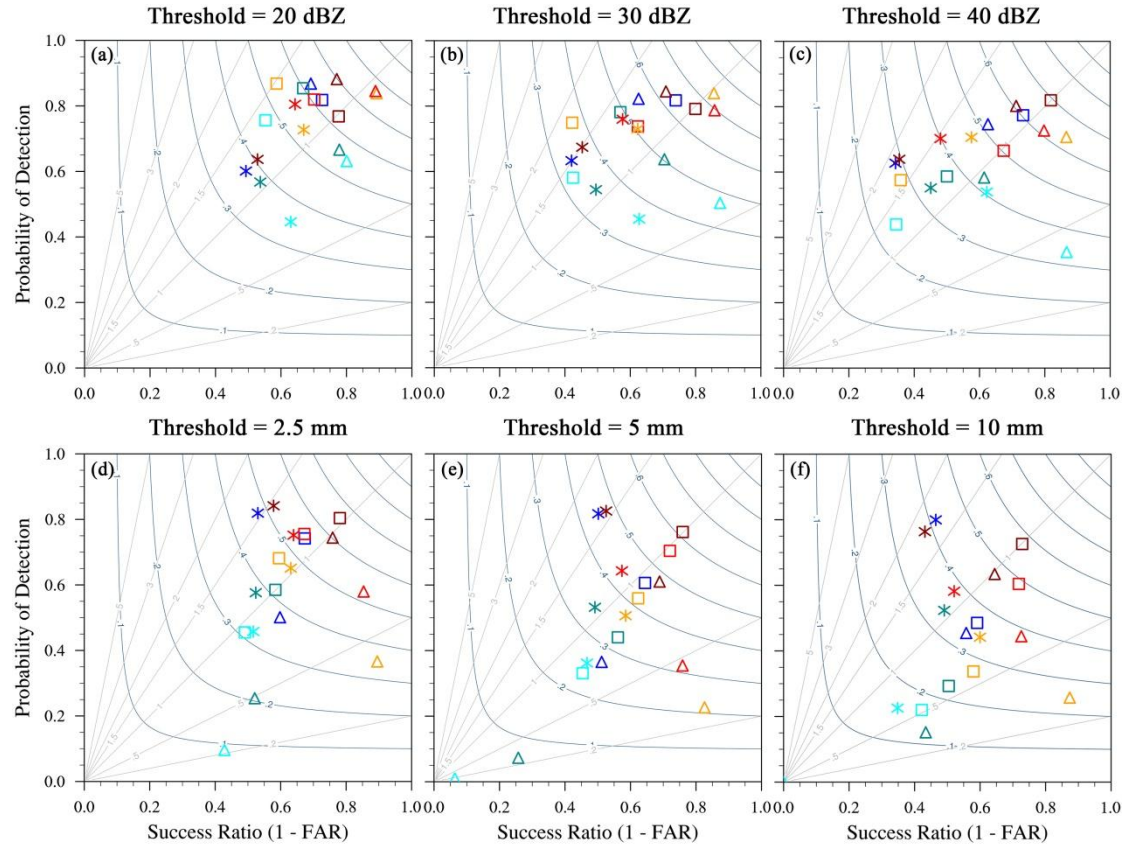
559 **Figure 15.** Performance diagram for 0-6 h CREF forecasts from the NoDA (cyan, dark cyan, and blue)

560 and FH_RD (orange, red, and brown) experiments in each case at thresholds of (a) 20, (b) 30, and (c)

561 40 dBZ, respectively. (d–f) Same as in (a–c), but for 1-6 h HPRCP forecasts from each case at

562 thresholds of (d) 2.5, (e) 5, and (f) 10 mm, respectively. Cyan and orange represent the analysis (1-h

563 forecast for precipitation), dark cyan and red for 3-h forecasts, and blue and brown for 6-h forecasts.

564 Results are shown for a neighborhood radius of 12-km.

565 To gain a comprehensive view of assimilating RWPs from multiple networks, quantitative

566 verification parameters (POD, BIAS, FAR, and CSI) from each case are aggregated across all available

567 forecast times. Figures 16 and 17 display time series of aggregated metrics for CREF forecasts from

568 NoDA, CTL, FH, RD, FH_RD, FH_RD_V120, FH_RD_H3, and FH_RD_H12 experiments at 20- and

569 40-dBZ thresholds, respectively. The error bars for NoDA, CTL, FH, RD, and FH_RD in the graphs

570 represent a 95% confidence interval. Compared to NoDA, all DA experiments exhibit more skillful

571   0–6h reflectivity forecasts, with higher POD and CSI, and smaller FAR. The BIAS values of the

572   assimilation experiments are higher than that of the NoDA experiment (close to unity) at the analysis

573   time, and then decreases slightly in the 1-6 h forecasts. However, the BIAS of NoDA increase

574   consistently during 1–6 hours, making it farther from unity. Among CTL, FH, RD, and FH_RD,

575   FH_RD consistently outperforms others, showing the highest POD values across all forecast hours (Fig.

576   16a). A slight overprediction bias (1.1–1.2) is observed for all DA experiments at all forecast times

577   (Fig. 16b). CTL exhibits the largest BIAS in the first 3 hours, while FH's BIAS increases to 1.2 over

578   time. FH_RD shows the steepest decrease in FAR, indicating the most effective reduction in false

579   alarms (Fig. 16c). CTL remains relatively flat and maintains the highest FAR among the four DA

580   experiments throughout the 0–6h forecasts. The FARs for FH and RD forecasts fall between those of

581   FH_RD and CTL. Specifically, FH has a lower FAR in the first 3 hours, whereas in the next 3 hours,

582   RD performs better. Similar trend is also evident in CSI values over time (Fig. 16d). In conclusion,

583   FH_RD consistently performs best overall across all metrics, followed by RD and FH. CTL

584   underperforms, with less improvement in score metrics. Sensitivity tests show FH_RD_H12 performs

585   slightly better than FH_RD, while FH_RD_H3 shows the least improvement. FH_RD_V120 falls

586   between FH_RD_H12 and FH_RD_H3, consistent with the single-case study in Sect. 4.1.3.
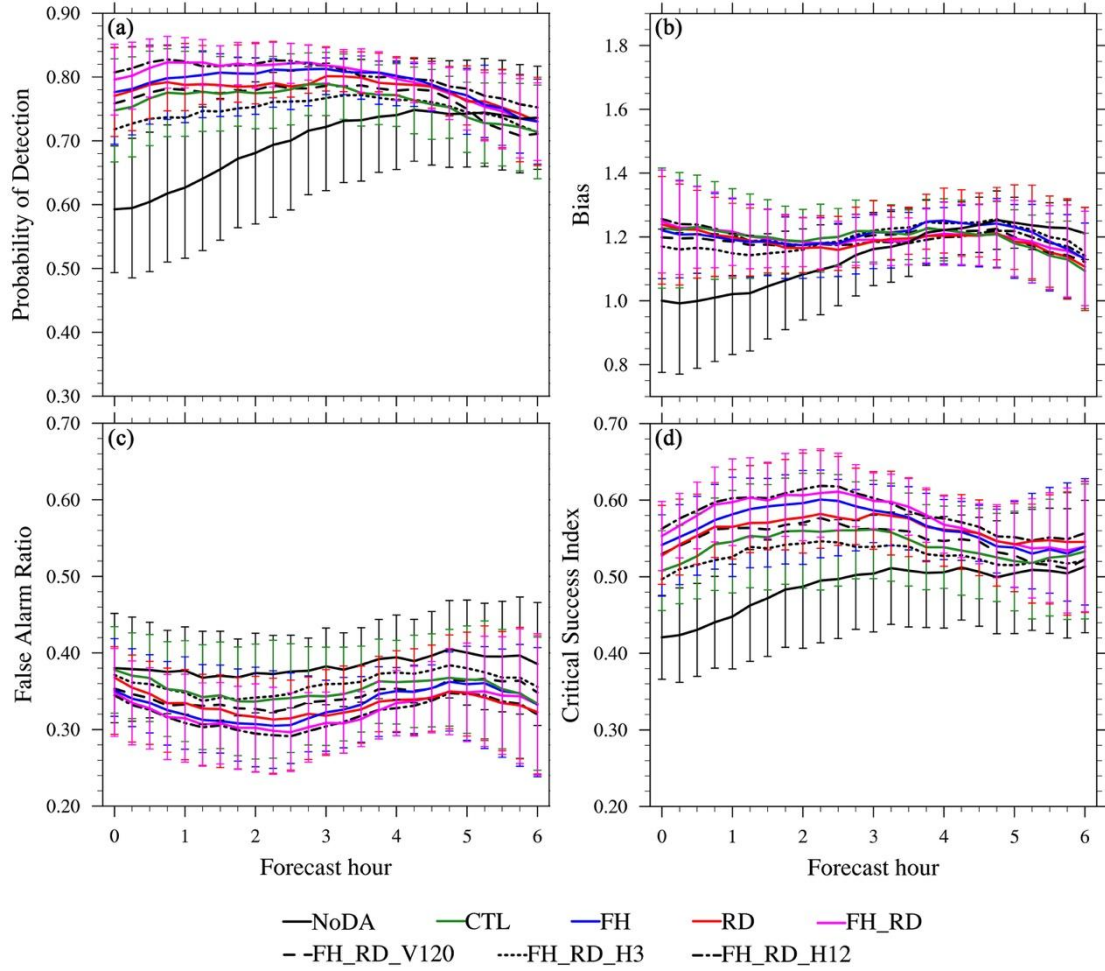
Figure 16. Time series of (a) Probability of detection (POD), (b) Bias, (c) false alarm ratio (FAR), and (d) critical success index (CSI) for CREF forecasts aggregated from each initialization hour from the sixth hour to the end of the DA cycles across three cases (June 28, July 12, July 21 of 2023) at the threshold of 20 dBZ for the NoDA (black solid), CTL (green solid), FH (blue solid), RD (red solid), FH_RD (magenta solid), FH_RD_V120 (black dashed), FH_RD_H3 (black dotted), and FH_RD_H12 (black dashdot) experiments. Results are shown for a neighborhood radius of 12-km. Error bars for NoDA, CTL, FH, RD, and FH_RD experiments represent a 95% confidence interval.

Similar to the 20-dBZ reflectivity forecast, RWP DA experiments outperform NoDA at 40-dBZ, although only the POD result in the first 3 hours is statistically significant at the 95% confidence level. All DA experiments exhibit an overprediction bias (1.1–1.5) throughout the 0–6 h forecasts (Fig. 17b). Notably, FH shows the highest bias. However, FH also exhibits the highest POD in the first 2 hours and highest CSI and lowest FAR in the first hour. Subsequently, FH_RD and RD perform better, with FH_RD slightly outperforming RD in 1–3 h forecasts and RD performing better in 4–6 hours. The different impacts of ridge and foothill networks may be attributed to: a) For southwest-type rainfall

602   events, the southwesterly wind propagates from upstream ridge stations to downstream foothill sites (Li

603   et al., 2024). b) Dynamic forcing of terrain, which has a delayed effect on triggering and intensifying

604   storms, leading to improved forecasts for later-occurring storms. c) Assimilating wind observations at

605   foothills, capturing local southwesterly flow characteristics, enhances forecasts of initial moisture

606   lifting and convection triggering. During the first 45 minutes, strong overprediction leads to high FARs,

607   which quickly decline as the forecast progresses (Fig. 17a and c). This contributes to an increase in CSI

608   (Fig. 17d). A possible reason is that the model requires time (several minutes to an hour) to digest and

609   adjust to assimilated wind information. The impact of vertical resolution and detection height on

610   40-dBZ reflectivity forecasts is consistent with the results observed at the 20-dBZ threshold.

611
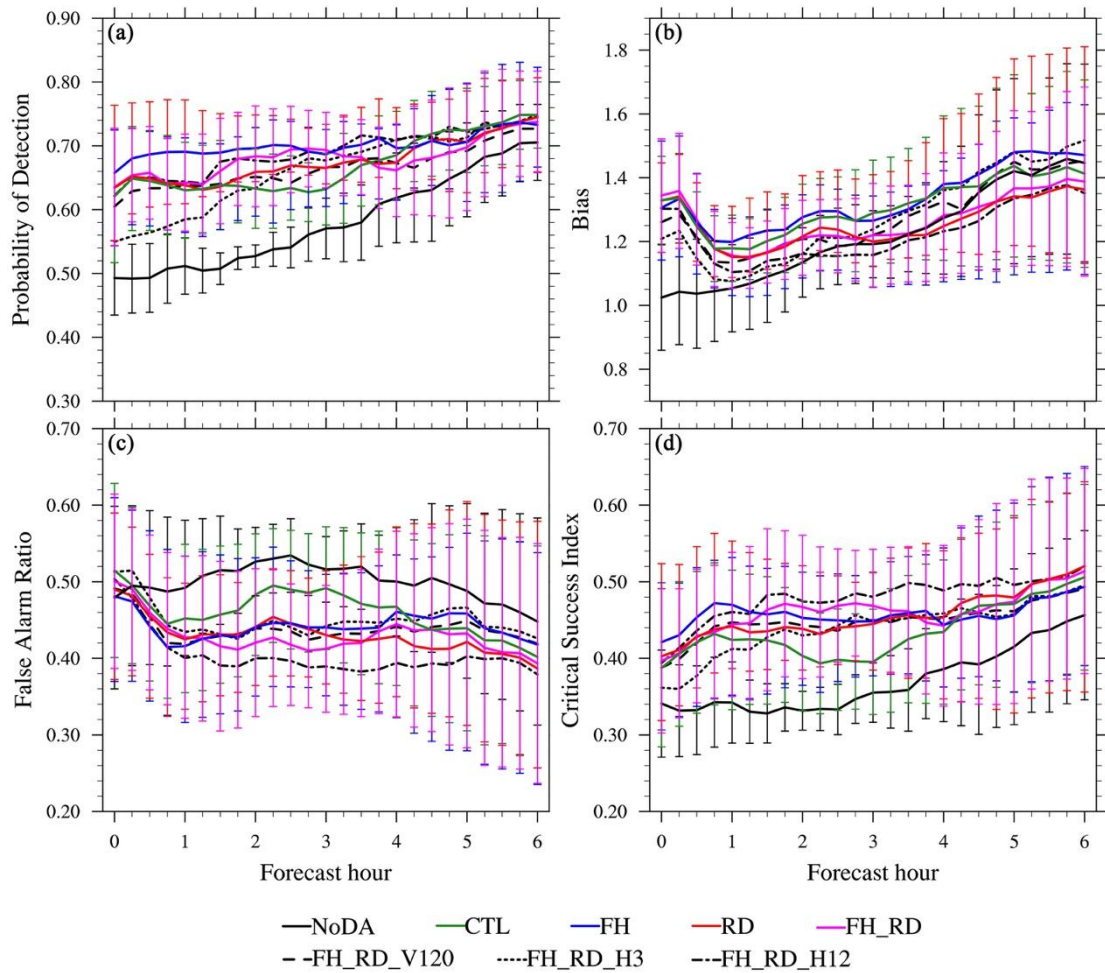
612   **Figure 17.** Same as in Figure 16, but for CREF forecasts at the threshold of 40 dBZ.

613   Consistent with the 20-dBZ reflectivity forecast, FH_RD and FH_RD_H12 consistently achieve

614   the best performance across all score metrics in HPRCP forecasts, followed by RD and FH (Fig. 18 and

615   19). Although the improvements are not statistically significant at the 95% confidence level, FH_RD

616   and FH_RD_H12 exhibit added forecast skill over the NoDA experiment. In contrast, CTL and

617 FH_RD_H3 show minimal improvement across all metrics. At 10-mm threshold, FH produces higher

618 forecast scores than the others in the first hour, while FH_RD and RD show superiority in 2–4 h and

619 4–6 h, respectively (Fig. 19).
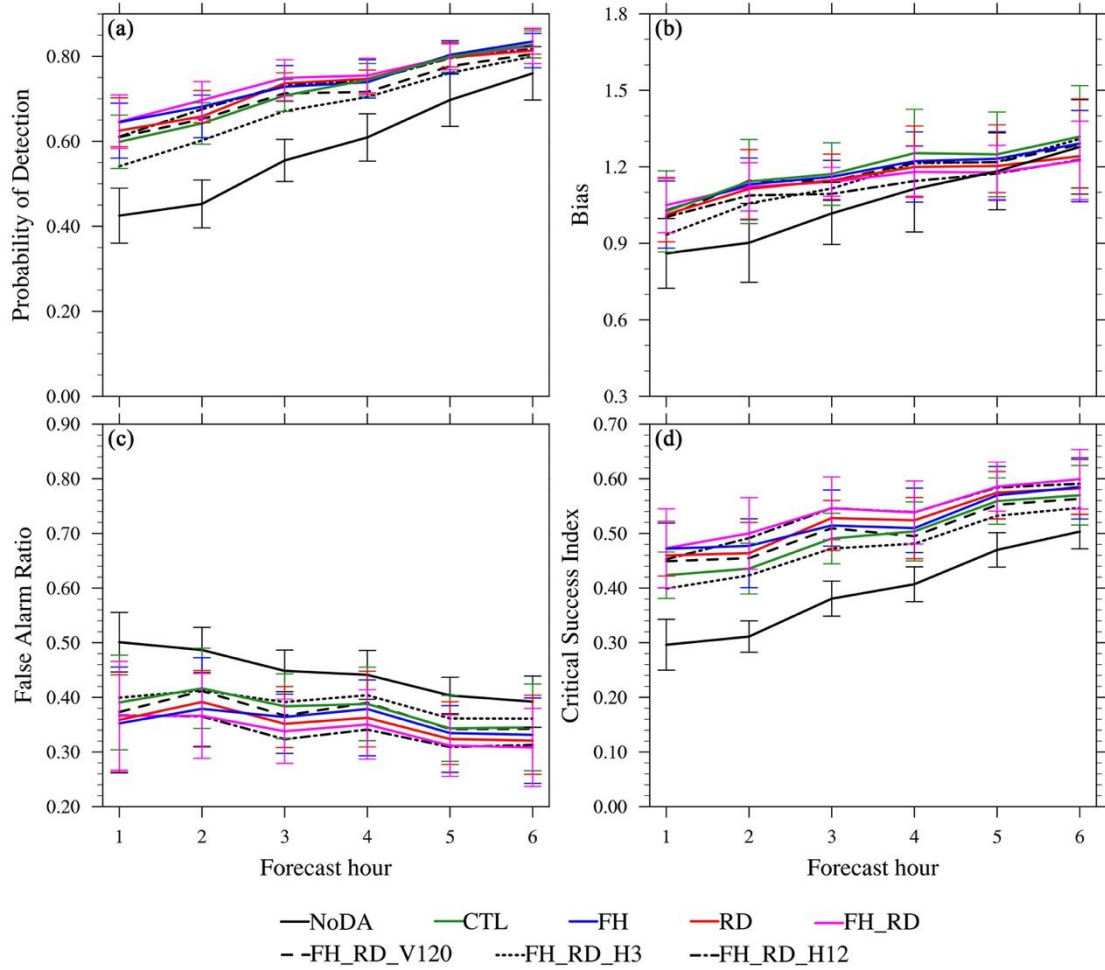
620

621 **Figure 18.** Same as in Figure 16, but for 1-6 h HPRCP forecasts aggregated from three cases at the

622 thresholds of 2.5 mm.
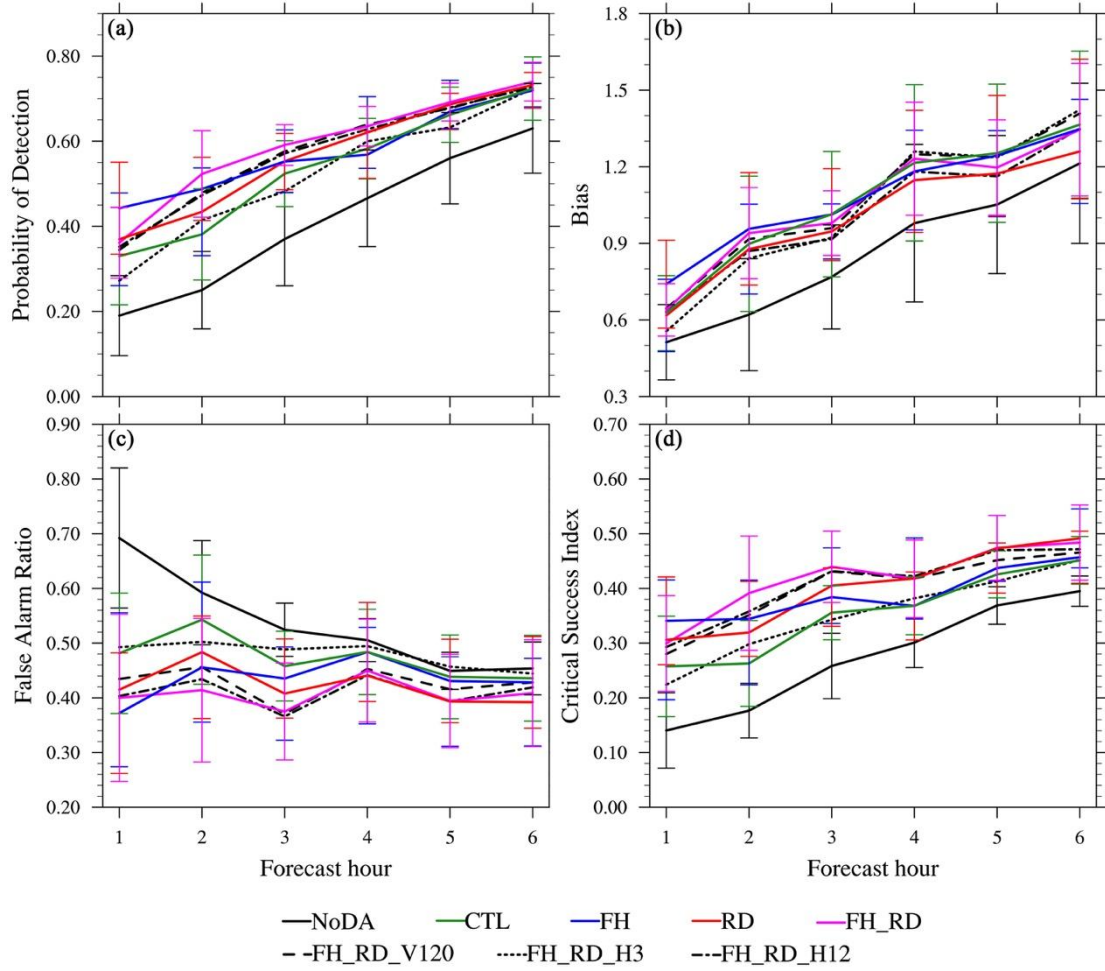
Figure 19. Same as in Figure 18, but for precipitation forecasts at the threshold of 10 mm.

5. Summary and conclusions

In this research, observing system simulation experiments are performed to study the benefits of assimilating RWP observations for convective scale short-term heavy rainfall forecasts. Synthetic RWP observations are assimilated into the WRF model using the NSSL3DVAR DA system for three SW-type heavy rainfall events that occurred over the Beijing-Tianjin-Hebei region. To investigate the impact of RWP data observed from multiple networks on convective scale short-term forecasts, the background run (NoDA), which does not assimilate any observations, and four types of DA experiments are carried out. A baseline experiment (CTL), which assimilates RWPs from the operational network alone, is first performed and serves as a benchmark for comparison with subsequent DA experiments. The FH and RD experiments assimilate simulated RWP observations from the foothill and ridge networks of the Taihang Mountains in addition to the operational network.

The FH_RD experiment is conducted by assimilating combined RWP data from the operational, foothill, and ridge sites. Comparison of analyses and forecasts from these four types of experiments reveals improvements in model initial conditions and short-term severe weather forecasts by assimilating simulated RWP observations, as well as the added value of RWPs from the foothill and ridge networks over operational network data. Furthermore, three sensitivity DA experiments (FH_RD_V120, FH_RD_H3, and FH_RD_H12) are carried out to test the impact of vertical resolution and maximum detection heights. The purpose of these experiments is to investigate a potential optimal configuration for the vertical data availability of real-time RWPs to be assimilated in future convective scale NWP. For each DA experiment, the analysis is cycled for 9 hours at 15-min intervals, with a 6-h free forecast initiated every hour starting from the sixth hour of the analysis cycles. First of all, both subjective and objective verifications of the analysis and forecast were performed in detail for the 21 July 2023 case. Then statistical metrics, including neighborhood-based POD, FAR, BIAS, and CSI of reflectivity and precipitation forecasts, were aggregated from each initialization hour across the three cases. The main results are summarized as follows:

1) Comparison of wind analyses and forecasts among the CTL, FH, RD, and FH_RD experiments reveals that the FH_RD experiment yields the smallest wind errors, both in terms of the overall domain average and the vertical profile of RMSEs for wind components. Then, it is followed by RD, then FH, with CTL exhibiting the largest wind errors. A qualitative evaluation of the model's initial mesoscale dynamics indicates that the assimilation of RWP data successfully corrects the wind direction and speed biases in Beijing and its surrounding areas, enhancing the southwesterly jet. Moreover, both RD and FH_RD (with the assimilation of RWP data from the ridge network) remarkably reduce large wind errors in the upstream of Beijing along the mountains, which is crucial for CI in the vicinity of the boundary between Hebei and southwestern Beijing.

2) For the 21 July 2023 event, qualitative verification focused on the convective system initiated southwest of Beijing, which intensified after merging with storms from western Hebei, forming a prominent southwest-northeast oriented system across Beijing. The NoDA experiment initially underestimates convection in Beijing and Hebei but overpredicts storm coverage and intensity in later forecasts, generating excessive spurious convection. All RWP DA experiments enhance CI timing and location by capturing mesoscale flow features, subsequently reducing storm

displacement and intensity errors. Nevertheless, the CTL experiment underestimates storm intensity, while FH still retains some spurious echoes in forecasts. Overall, the FH_RD experiment demonstrates significant superiority in areal coverage, storm mode, and orientation compared to the other DA experiments. The accumulated precipitation forecasts show similar trends to the reflectivity results regarding rainfall location, onset time, and amount. The forecast statistics indicate that FH_RD achieves the best performance in reflectivity and precipitation forecasts at lower thresholds (i.e., 20- and 30-dBZ for CREF, and 2.5-mm for HPRCP), whereas the RD experiment slightly surpasses FH_RD at the 50-dBZ and 10-mm thresholds. The lower performance of FH_RD and FH at higher thresholds may be linked to slight displacement errors in heavy precipitation forecasts, impacting their POD and ETS scores.

3) Quantitative verification results aggregated across the three SW-type heavy rainfall cases in the Beijing-Tianjin-Hebei region confirm that FH_RD exhibits the best performance in reflectivity and precipitation forecasts, followed by RD and FH, while CTL shows minimal improvement. An exception is that at higher thresholds, FH achieves the best scores in the first 1 or 2 hours despite stronger overprediction, while FH_RD and RD are superior in subsequent hours. This is potentially attributed to the delayed effect of dynamic forcing from the terrain, as well as improvements in capturing the initial southwesterly flow and local convection by assimilating wind observations at the foothills. In addition, the results from sensitivity experiments on vertical resolution and maximum detection height indicate that FH_RD_H12 exhibits comparable or slightly better performance compared to FH_RD, benefiting from its higher detection height. Conversely, the FH_RD_H3 experiment, with the lowest detection height, has the poorest forecast skills among all DA experiments, while FH_RD_V120 generally falls between FH_RD_H12 and FH_RD_H3.

The results consistently demonstrate that the FH_RD experiment, combining data from ridge, foothill, and operational wind profiler networks, delivers the most accurate short-term forecasts. Specifically, the assimilation of RWP data from ridge network significantly reduces wind errors in complex terrain, such as the Taihang Mountains upstream of Beijing. These regions are critical for convective initiation in Beijing and its surroundings. The findings highlight the essential role of integrating both ridge and foothill data in improving overall reflectivity and precipitation forecasts over the Beijing-Tianjin-Hebei region. Sensitivity experiments on vertical resolution and detection height

696 further emphasize the importance of high vertical resolution and maximizing detection height in
697 optimizing the RWP network for enhanced forecast accuracy.

698   The insights gained from this OSSE study on the impacts of RWP observations on heavy rainfall
699 forecasting will inform the design of optimal RWP networks over the Beijing-Tianjin-Hebei region.
700 This preliminary study lays the groundwork for further research to fully understand the complexities of
701 precipitation forecasting related to data assimilation. The current investigation focused on three
702 SW-type heavy rainfall cases occurring in summer over the Beijing-Tianjin-Hebei region, utilizing
703 model-simulated states and observational networks. As the fraternal twin scheme is used in this study,
704 it does not account for model-related errors that occur in real-world applications. Consequently, the
705 results might overestimate the actual benefits of RWP assimilation in operational systems. Furthermore,
706 this study focuses exclusively on assimilating RWP data, without incorporating conventional
707 observations or satellite data. While this approach simplifies the analysis by isolating the impact of
708 RWPs, it may inflate their relative importance. Future research directions include: (1) Expanding the
709 study to other precipitation types and high-impact convective events under diverse weather scenarios.
710 (2) Evaluating the impact of RWP networks by assimilating RWPs together with more diverse
711 observation types and incorporating non-identical twin setups to enhance realism and provide broader
712 operational insights. (3) Investigating the benefits of assimilating real observational data on convective
713 scale NWP once proposed RWP networks become available. Moreover, future studies can address the
714 limitations of static background errors in 3DVAR by incorporating flow-dependent background error
715 covariances estimated from ensemble forecasts. As ensemble-based background error covariances can
716 dynamically adapt to the evolving state of the atmosphere, the DA system will better represent the
717 spatial and temporal variability of background errors, particularly in regions with complex topography
718 or mesoscale features like convective systems. By leveraging flow-dependent background errors, the
719 analysis can more accurately capture the initial atmospheric state, ultimately leading to more accurate
720 precipitation predictions.

721

Code and data availability

The WRF model may be downloaded from https://github.com/wrf-model (WRF, 2023). The ERA5 reanalysis and GFS forecast data are accessible from ECMWF (https://www.ecmwf.int/en/forecasts/datasets/reanalysis-datasets/era5/) and National Centers for Environmental Prediction, National Weather Service, NOAA, U.S. Department of Commerce (https://rda.ucar.edu/datasets/d084003/dataaccess/), respectively. The source code for WRF model version 3.7.1, and the input ERA5 and GFS data used in this study have been archived on Zenodo at https://doi.org/10.5281/zenodo.14321805. The namelist files for WRF and the assimilation system used in this study are accessible online (https://doi.org/10.5281/zenodo.14241597).

Author contributions

JZ and JG conceptualized the study. JZ executed the experiments, analyzed the results, and wrote the paper. JG supervised the project, provided critical feedback during the experiment implemention stage, and revised the paper. XZ assisted in the analysis and visualizations.

Competing interests

The contact author has declared that none of the authors has any competing interests.

Acknowledgements

This work was jointly supported by the National Natural Science Foundation of China (U2142209, 42325501 and 42375018), and the China Meteorological Administration Training Centre Key Research Program (2023CMATCZDIAN08). Dr. Jidong Gao kindly provided internal review which led to improvement of the manuscript. ChatGPT (GPT-4; OpenAI's large-scale language-generation model) was used to improve the writing style of this article.

746   **References**

747   Amante, C. and Eakins, B. W.: ETOPO1 arc-minute global relief model : procedures, data sources and
748   analysis, 2009.

749   Benjamin, S. G., Grell, G. A., Brown, J. M., Smirnova, T. G., and Bleck, R.: Mesoscale Weather
750   Prediction with the RUC Hybrid Isentropic–Terrain-Following Coordinate Model, Monthly Weather
751   Review, 132, 473–494, https://doi.org/10.1175/1520-0493(2004)132<0473:MWPWTR>2.0.CO;2,
752   2004a.

753   Benjamin, S. G., Schwartz, B. E., Szoke, E. J., and Koch, S. E.: The Value of Wind Profiler Data in
754   U.S. Weather Forecasting, Bulletin of the American Meteorological Society, 85, 1871–1886,
755   https://doi.org/10.1175/BAMS-85-12-1871, 2004b.

756   Bouttier, F.: The use of profiler data at ECMWF, metz, 10, 497–510,
757   https://doi.org/10.1127/0941-2948/2001/0010-0497, 2001.

758   Bucci, L. R., Majumdar, S. J., Atlas, R., Emmitt, G. D., and Greco, S.: Understanding the response of
759   tropical cyclone structure to the assimilation of synthetic wind profiles, Monthly Weather Review,
760   https://doi.org/10.1175/MWR-D-20-0153.1, 2021.

761   Clark, A. J., Gallus, W. A., and Weisman, M. L.: Neighborhood-Based Verification of Precipitation
762   Forecasts from Convection-Allowing NCAR WRF Model Simulations and the Operational NAM,
763   Weather and Forecasting, 25, 1495–1509, https://doi.org/10.1175/2010WAF2222404.1, 2010.

764   Dudhia, J.: Numerical Study of Convection Observed during the Winter Monsoon Experiment Using a
765   Mesoscale Two-Dimensional Model, Journal of Atmospheric Sciences, 46, 3077–3107,
766   https://doi.org/10.1175/1520-0469(1989)046<3077:NSOCOD>2.0.CO;2, 1989.

767   Dunn, L.: An Example of Subjective Interpretation of Network Profiler Data in Real-Time Forecasting,
768   Weather and Forecasting, 1, 219–225,
769   https://doi.org/10.1175/1520-0434(1986)001<0219:AEOSIO>2.0.CO;2, 1986.

770   Fierro, A. O., Wang, Y., Gao, J., and Mansell, E. R.: Variational Assimilation of Radar Data and GLM
771   Lightning-Derived Water Vapor for the Short-Term Forecasts of High-Impact Convective Events,
772   Monthly Weather Review, 147, 4045–4069, https://doi.org/10.1175/MWR-D-18-0421.1, 2019a.

773   Fierro, A. O., Wang, Y., Gao, J., and Mansell, E. R.: Variational Assimilation of Radar Data and GLM
774   Lightning-Derived Water Vapor for the Short-Term Forecasts of High-Impact Convective Events,
775   Monthly Weather Review, 147, 4045–4069, https://doi.org/10.1175/MWR-D-18-0421.1, 2019b.

776   Gao, J. and Stensrud, D. J.: Assimilation of Reflectivity Data in a Convective-Scale, Cycled 3DVAR
777   Framework with Hydrometeor Classification, Journal of the Atmospheric Sciences, 69, 1054–1065,
778   https://doi.org/10.1175/JAS-D-11-0162.1, 2012.

779   Gao, J. and Stensrud, D. J.: Some Observing System Simulation Experiments with a Hybrid 3DEnVAR
780   System for Storm-Scale Radar Data Assimilation, Monthly Weather Review, 142, 3326–3346,
781   https://doi.org/10.1175/MWR-D-14-00025.1, 2014.

782   Gao, J., Xue, M., Brewster, K., and Droegemeier, K. K.: A Three-Dimensional Variational Data
783   Analysis Method with Recursive Filter for Doppler Radars, Journal of Atmospheric and Oceanic

784   Technology, 21, 457–469, https://doi.org/10.1175/1520-0426(2004)021<0457:ATVDAM>2.0.CO;2,
785   2004.

786   Gao, J., Smith, T. M., Stensrud, D. J., Fu, C., Calhoun, K., Manross, K. L., Brogden, J., Lakshmanan,
787   V., Wang, Y., Thomas, K. W., Brewster, K., and Xue, M.: A Real-Time Weather-Adaptive 3DVAR
788   Analysis System for Severe Weather Detections and Warnings, Weather and Forecasting, 28, 727–745,
789   https://doi.org/10.1175/WAF-D-12-00093.1, 2013.

790   Gao, J., Fu, C., Stensrud, D. J., and Kain, J. S.: OSSEs for an Ensemble 3DVAR Data Assimilation
791   System with Radar Observations of Convective Storms, Journal of the Atmospheric Sciences, 73,
792   2403–2426, https://doi.org/10.1175/JAS-D-15-0311.1, 2016.

793   Gao, J., Heinselman, L. P., Xue, M., Wicker, L. J., Yussouf, N., Stensrud, D. J., and Droegemeier, K.
794   K.: The Numerical Prediction of Severe Convective Storms: Advances in Research and Applications,
795   Remaining Challenges, and Outlook for the Future., in: Encyclopedia of Atmospheric Sciences,
796   Elsevier, 2024.

797   Ge, G., Gao, J., and Xue, M.: Diagnostic Pressure Equation as a Weak Constraint in a Storm-Scale
798   Three-Dimensional Variational Radar Data Assimilation System, Journal of Atmospheric and Oceanic
799   Technology, 29, 1075–1092, https://doi.org/10.1175/JTECH-D-11-00201.1, 2012.

800   Guo, X., Guo, J., Zhang, D., and Yun, Y.: Vertical divergence profiles as detected by two wind-profiler
801   mesonets over East China: Implications for nowcasting convective storms, Quart J Royal Meteoro Soc,
802   149, 1629–1649, https://doi.org/10.1002/qj.4474, 2023.

803   Heinselman, P. L., Burke, P. C., Wicker, L. J., Clark, A. J., Kain, J. S., Gao, J., Yussouf, N., Jones, T.
804   A., Skinner, P. S., Potvin, C. K., Wilson, K. A., Gallo, B. T., Flora, M. L., Martin, J., Creager, G.,
805   Knopfmeier, K. H., Wang, Y., Matilla, B. C., Dowell, D. C., Mansell, E. R., Roberts, B., Hoogewind,
806   K. A., Stratman, D. R., Guerra, J., Reinhart, A. E., Kerr, C. A., and Miller, W.: Warn-on-Forecast
807   System: From   Vision   to   Reality,   Weather   and   Forecasting,   39,   75–95,
808   https://doi.org/10.1175/WAF-D-23-0147.1, 2024.

809   Hersbach, H., Bell, B., Berrisford, P., Hirahara, S., Horányi, A., Muñoz-Sabater, J., Nicolas, J., Peubey,
810   C., Radu, R., Schepers, D., Simmons, A., Soci, C., Abdalla, S., Abellan, X., Balsamo, G., Bechtold, P.,
811   Biavati, G., Bidlot, J., Bonavita, M., De Chiara, G., Dahlgren, P., Dee, D., Diamantakis, M., Dragani,
812   R., Flemming, J., Forbes, R., Fuentes, M., Geer, A., Haimberger, L., Healy, S., Hogan, R. J., Hólm, E.,
813   Janisková, M., Keeley, S., Laloyaux, P., Lopez, P., Lupu, C., Radnoti, G., De Rosnay, P., Rozum, I.,
814   Vamborg, F., Villaume, S., and Thépaut, J.: The ERA5 global reanalysis, Quart J Royal Meteoro Soc,
815   146, 1999–2049, https://doi.org/10.1002/qj.3803, 2020.

816   Hoffman, R. N. and Atlas, R.: Future Observing System Simulation Experiments, Bulletin of the
817   American Meteorological Society, 97, 1601–1616, https://doi.org/10.1175/BAMS-D-15-00200.1, 2016.

818   Hoffmann, L., Günther, G., Li, D., Stein, O., Wu, X., Griessbach, S., Heng, Y., Konopka, P., Müller, R.,
819   Vogel, B., and Wright, J. S.: From ERA-Interim to ERA5: the considerable impact of ECMWF's
820   next-generation reanalysis on Lagrangian transport simulations, Atmos. Chem. Phys., 19, 3097–3124,
821   https://doi.org/10.5194/acp-19-3097-2019, 2019.

822   Hong, S.-Y., Noh, Y., and Dudhia, J.: A New Vertical Diffusion Package with an Explicit Treatment of

Entrainment Processes, Monthly Weather Review, 134, 2318–2341, https://doi.org/10.1175/MWR3199.1, 2006.

Hu, H., Sun, J., and Zhang, Q.: Assessing the Impact of Surface and Wind Profiler Data on Fog Forecasting Using WRF 3DVAR: An OSSE Study on a Dense Fog Event over North China, Journal of Applied Meteorology and Climatology, 56, 1059–1081, https://doi.org/10.1175/JAMC-D-16-0246.1, 2017.

Hu, J., Fierro, A. O., Wang, Y., Gao, J., and Mansell, E. R.: Exploring the Assimilation of GLM-Derived Water Vapor Mass in a Cycled 3DVAR Framework for the Short-Term Forecasts of High-Impact Convective Events, Monthly Weather Review, 148, 1005–1028, https://doi.org/10.1175/MWR-D-19-0198.1, 2020.

Hu, J., Gao, J., Wang, Y., Pan, S., Fierro, A. O., Skinner, P. S., Knopfmeier, K., Mansell, E. R., and Heinselman, P. L.: Evaluation of an experimental WARN-ON-FORECAST 3DVAR analysis and forecast system on quasi-real-time short-term forecasts of high-impact weather events, QJR Meteorol Soc, 147, 4063–4082, https://doi.org/10.1002/qj.4168, 2021.

Huang, Y., Wang, X., Kerr, C., Mahre, A., Yu, T.-Y., and Bodine, D.: Impact of Assimilating Future Clear-Air Radial Velocity Observations from Phased-Array Radar on a Supercell Thunderstorm Forecast: An Observing System Simulation Experiment Study, Monthly Weather Review, 148, 3825–3845, https://doi.org/10.1175/MWR-D-19-0391.1, 2020.

Huang, Y., Wang, X., Mahre, A., Yu, T.-Y., and Bodine, D.: Impacts of assimilating future clear-air radial velocity observations from phased array radar on convection initiation forecasts: An observing system simulation experiment study, Monthly Weather Review, https://doi.org/10.1175/MWR-D-21-0199.1, 2022.

Huo, Z., Liu, Y., Shi, Y., Chen, B., Fan, H., and Li, Y.: An Investigation on Joint Data Assimilation of a Radar Network and Ground-Based Profiling Platforms for Forecasting Convective Storms, Monthly Weather Review, 151, 2049–2064, https://doi.org/10.1175/MWR-D-22-0332.1, 2023.

Ishihara, M., Kato, Y., Abo, T., Kobayashi, K., and Izumikawa, Y.: Characteristics and Performance of the Operational Wind Profiler Network of the Japan Meteorological Agency, Journal of the Meteorological Society of Japan, 84, 1085–1096, https://doi.org/10.2151/jmsj.84.1085, 2006.

Jones, T. A., Wang, X., Skinner, P., Johnson, A., and Wang, Y.: Assimilation of GOES-13 Imager Clear-Sky Water Vapor (6.5 μm) Radiances into a Warn-on-Forecast System, Monthly Weather Review, 146, 1077–1107, https://doi.org/10.1175/MWR-D-17-0280.1, 2018.

Li, N., Guo, J., Wu, M., Zhang, F., Guo, X., Sun, Y., Zhang, Z., Liang, H., and Chen, T.: Low-Level Jet and Its Effect on the Onset of Summertime Nocturnal Rainfall in Beijing, Geophysical Research Letters, 51, e2024GL110840, https://doi.org/10.1029/2024GL110840, 2024.

Liu, B., Guo, J., Gong, W., Shi, L., Zhang, Y., and Ma, Y.: Characteristics and performance of wind profiles as observed by the radar wind profiler network of China, Atmos. Meas. Tech., 13, 4589–4600, https://doi.org/10.5194/amt-13-4589-2020, 2020.

Liu, D., Huang, C., and Feng, J.: Influence of Assimilating Wind Profiling Radar Observations in Distinct Dynamic Instability Regions on the Analysis and Forecast of an Extreme Rainstorm Event in

862   Southern China, Remote Sensing, 14, 3478, https://doi.org/10.3390/rs14143478, 2022.

863   Mallick, S. and Jones, T. A.: Assimilation of GOES-16 satellite derived winds into the
864   warn-on-forecast   system,   Atmospheric   Research,   245,   105131,
865   https://doi.org/10.1016/j.atmosres.2020.105131, 2020.

866   Mansell, E. R. and Ziegler, C. L.: Aerosol Effects on Simulated Storm Electrification and Precipitation
867   in a Two-Moment Bulk Microphysics Model, Journal of the Atmospheric Sciences, 70, 2032–2050,
868   https://doi.org/10.1175/JAS-D-12-0264.1, 2013.

869   Mansell, E. R., Ziegler, C. L., and Bruning, E. C.: Simulated Electrification of a Small Thunderstorm
870   with Two-Moment Bulk Microphysics, Journal of the Atmospheric Sciences, 67, 171–194,
871   https://doi.org/10.1175/2009JAS2965.1, 2010.

872   Mlawer, E. J., Taubman, S. J., Brown, P. D., Iacono, M. J., and Clough, S. A.: Radiative transfer for
873   inhomogeneous atmospheres: RRTM, a validated correlated-k model for the longwave, J. Geophys.
874   Res., 102, 16663–16682, https://doi.org/10.1029/97JD00237, 1997.

875   Pan, S., Gao, J., Stensrud, D. J., Wang, X., and Jones, T. A.: Assimilation of Radar Radial Velocity and
876   Reflectivity, Satellite Cloud Water Path, and Total Precipitable Water for Convective-Scale NWP in
877   OSSEs,   Journal   of   Atmospheric   and   Oceanic   Technology,   35,   67–89,
878   https://doi.org/10.1175/JTECH-D-17-0081.1, 2018.

879   Pan, S., Gao, J., Jones, T. A., Wang, Y., Wang, X., and Li, J.: The Impact of Assimilating
880   Satellite-Derived Layered Precipitable Water, Cloud Water Path, and Radar Data on Short-Range
881   Thunderstorm   Forecasts,   Monthly   Weather   Review,   149,   1359–1380,
882   https://doi.org/10.1175/MWR-D-20-0040.1, 2021.

883   Potvin, C. K. and Flora, M. L.: Sensitivity of Idealized Supercell Simulations to Horizontal Grid
884   Spacing: Implications for Warn-on-Forecast, Monthly Weather Review, 143, 2998–3024,
885   https://doi.org/10.1175/MWR-D-14-00416.1, 2015.

886   Purser, R. J., Wu, W.-S., Parrish, D. F., and Roberts, N. M.: Numerical Aspects of the Application of
887   Recursive Filters to Variational Statistical Analysis. Part I: Spatially Homogeneous and Isotropic
888   Gaussian   Covariances,   Monthly   Weather   Review,   131,   1524–1535,
889   https://doi.org/10.1175//1520-0493(2003)131<1524:NAOTAO>2.0.CO;2, 2003a.

890   Purser, R. J., Wu, W. S., Parrish, D. F., and Roberts, N. M.: Numerical Aspects of the Application of
891   Recursive Filters to Variational Statistical Analysis. Part II: Spatially Inhomogeneous and Anisotropic
892   General Covariances, Monthly Weather Review, 131, 1536–1548, 2003b.

893   Sheng, J., Zheng, Y., and Shen, X.: Climatology and environmental conditions of two types of
894   quasi-linear convective systems with extremely intense weather in North China, Acta Meteorologica
895   Sinica, 78(6), 877–898, 2020.

896   Shu-yuan, L., Yongguang, Z., and Zuyu, T.: The analysis of the relationship between pulse of LLJ and
897   heavy rain using wind profiler data, Journal of tropical meteorology, 2003.

898   Skamarock, W., Klemp, J., Dudhia, J., Gill, D., Barker, D., Wang, W., Huang, X.-Y., and Duda, M.: A
899   Description   of   the   Advanced   Research   WRF   Version   3,   UCAR/NCAR,

900   https://doi.org/10.5065/D68S4MVH, 2008.

901   St-James, J. S. and Laroche, S.: Assimilation of Wind Profiler Data in the Canadian Meteorological
902   Centre's Analysis Systems, Journal of Atmospheric and Oceanic Technology, 22, 1181–1194,
903   https://doi.org/10.1175/JTECH1765.1, 2005.

904   Wang, C., Chen, Y., Chen, M., and Shen, J.: Data assimilation of a dense wind profiler network and its
905   impact   on   convective   forecasting,   Atmospheric   Research,   238,   104880,
906   https://doi.org/10.1016/j.atmosres.2020.104880, 2020.

907   Wang, C., Chen, M., and Chen, Y.: Impact of Combined Assimilation of Wind Profiler and Doppler
908   Radar Data on a Convective-Scale Cycling Forecasting System, Monthly Weather Review, 150,
909   431–450, https://doi.org/10.1175/MWR-D-20-0383.1, 2022.

910   Wang, C., Chen, Y., Chen, M., and Huang, X.-Y.: Evaluation of two observation operator schemes for
911   wind profiler radar data assimilation and its impacts on short-term forecasting, Atmospheric Research,
912   283, 106549, https://doi.org/10.1016/j.atmosres.2022.106549, 2023a.

913   Wang, S., Guo, J., Xian, T., Li, N., Meng, D., Li, H., and Cheng, W.: Investigation of low-level
914   supergeostrophic wind and Ekman spiral as observed by a radar wind profiler in Beijing, Front.
915   Environ. Sci., 11, 1195750, https://doi.org/10.3389/fenvs.2023.1195750, 2023b.

916   Wang, Y., Gao, J., Skinner, P. S., Knopfmeier, K., Jones, T., Creager, G., Heiselman, P. L., and Wicker,
917   L. J.: Test of a Weather-Adaptive Dual-Resolution Hybrid Warn-on-Forecast Analysis and Forecast
918   System for Several Severe Weather Events, Weather and Forecasting, 34, 1807–1827,
919   https://doi.org/10.1175/WAF-D-19-0071.1, 2019.

920   Zhang, L. and Pu, Z.: An Observing System Simulation Experiment (OSSE) to Assess the Impact of
921   Doppler Wind Lidar (DWL) Measurements on the Numerical Simulation of a Tropical Cyclone,
922   Advances in Meteorology, 2010, 743863, https://doi.org/10.1155/2010/743863, 2010.

923   Zhang, X., Luo, Y., Wan, Q., Ding, W., and Sun, J.: Impact of Assimilating Wind Profiling Radar
924   Observations on Convection-Permitting Quantitative Precipitation Forecasts during SCMREX,
925   Weather and Forecasting, 31, 1271–1292, https://doi.org/10.1175/WAF-D-15-0156.1, 2016.

926   Zhang, Y., Chen, M., and Zhong, J.: A Quality Control Method for Wind Profiler Observations toward
927   Assimilation Applications, Journal of Atmospheric and Oceanic Technology, 34, 1591–1606,
928   https://doi.org/10.1175/JTECH-D-16-0161.1, 2017.

929   Zhao, J., Gao, J., Jones, T. A., and Hu, J.: Impact of Assimilating High-Resolution Atmospheric
930   Motion Vectors on Convective Scale Short-Term Forecasts: 1. Observing System Simulation
931   Experiment (OSSE), Journal of Advances in Modeling Earth Systems, 13, e2021MS002484,
932   https://doi.org/10.1029/2021MS002484, 2021a.

933   Zhao, J., Gao, J., Jones, T. A., and Hu, J.: Impact of Assimilating High-Resolution Atmospheric
934   Motion Vectors on Convective Scale Short-Term Forecasts: 2. Assimilation Experiments of GOES-16
935   Satellite Derived Winds, Journal of Advances in Modeling Earth Systems, 13, e2021MS002486,
936   https://doi.org/10.1029/2021MS002486, 2021b.

937   Zhao, J., Gao, J., Jones, T., and Hu, J.: Impact of Assimilating High-Resolution Atmospheric Motion

938   Vectors on Convective Scale Short-Term Forecasts: 3. Experiments With Radar Reflectivity and Radial
939   Velocity, Journal of Advances in Modeling Earth Systems, 14, e2022MS003246,
940   https://doi.org/10.1029/2022MS003246, 2022.

941   Zhao, N., Yue, T., Li, H., Zhang, L., Yin, X., and Liu, Y.: Spatio-temporal changes in precipitation
942   over Beijing-Tianjin-Hebei region, China, Atmospheric Research, 202, 156–168,
943   https://doi.org/10.1016/j.atmosres.2017.11.029, 2018.

944   Zhong, S., Fast, J. D., and Bian, X.: A Case Study of the Great Plains Low-Level Jet Using Wind
945   Profiler Network Data and a High-Resolution Mesoscale Model, Monthly Weather Review, 124,
946   785–806, https://doi.org/10.1175/1520-0493(1996)124<0785:ACSOTG>2.0.CO;2, 1996.

947   Zhou, S., Yang, J., Wang, W., Gong, D., Shi, P., and Gao, M.: Shift of daily rainfall peaks over the
948   Beijing–Tianjin–Hebei region: An indication of pollutant effects?, Intl Journal of Climatology, 38,
949   5010–5019, https://doi.org/10.1002/joc.5700, 2018.

950   Zhuang, Z., Yussouf, N., and Gao, J.: Analyses and forecasts of a tornadic supercell outbreak using a
951   3DVAR system ensemble, Advances in Atmospheric Sciences, 33, 544–558,
952   https://doi.org/10.1007/s00376-015-5072-0, 2016.

953   Ziegler, C. L.: Retrieval of Thermal and Microphysical Variables in Observed Convective Storms. Part
954   1: Model Development and Preliminary Testing, Journal of Atmospheric Sciences, 42, 1487–1509,
955   https://doi.org/10.1175/1520-0469(1985)042<1487:ROTAMV>2.0.CO;2, 1985.

956